Dalton Transactions

ROYAL SOCIETY OF CHEMISTRY

PAPER

Published on 09 October 2026
Licensed under CC-BY-NC 4.0

Check for updates

Cite this: DOI: 10.1039/d6dt01814a

Trigonal antiprismatic Co^{II} complexes: why don't they work like single-molecule magnets in a zero-field?

Aritz Landart-Gereka, [a] Pedro J. Jabalera-Ortiz,[a] Laura Cuevas-Contreras,[a] J. Krzystek,[b] Mykhaylo Ozerov, [b] Maria Mar Quesada-Moreno, [c] Maria A. Palacios *[a] and Enrique Colacio *[a]

This paper describes the synthesis, crystal structures, detailed dc and ac magnetic properties, far-infrared magnetic spectroscopy (FIRMS), and theoretical calculations of two further examples of the scarce trigonal antiprismatic Co^{II} complexes (octahedral complexes distorted along the C_3 axis). One has been prepared from the scorpionate ligand hydridotris(1,2,4-triazolyl)borate (Ttz^-) and the other from the tridentate bridging ligand 1-methylimidazole-2-carboxamide oxime (HL). The first complex has the formula $[Co^{II}(Ttz)_2]\cdot 5.5H_2O$ (**1**), whereas the second, $[Co_3(L)_6](NO_3)_2\cdot 6H_2O$ (**2**), is a mixed-valence Co^{III}–Co^{II}–Co^{III} trinuclear complex. In **1**, the pseudo-C_3 axis of the trigonal antiprismatic high spin $Co^{II}N_6$ coordination sphere lies along the B···Co···B direction, whereas in **2** the C_3 axis of the $Co^{II}O_6$ unit lies along the $Co^{III}Co^{II}Co^{III}$ direction. Although both complexes exhibit very strong easy-axis magnetic anisotropy, they do not show slow magnetic relaxation under zero field but rather behave like field-induced single-ion magnets (SIMs). Experimental and theoretical magneto-structural correlations carried out on all the trigonal antiprismatic Co^{II} complexes reported to date, as well as on related model complexes, confirm, on the one hand, that the axiality g_{xy}/g_z increases when the s/h ratio decreases, that is to say when the compounds are more elongated along the C_3 or pseudo C_3 axis, and on the other hand, that all of them exhibit easy-axis magnetic anisotropy but with significant intrinsic transversal anisotropy ($g_{xy}/g_z > 0.1$), which prevents SIM behaviour in a zero-field. Furthermore, the results of the theoretical studies suggest that the use of neutral ligands based on scorpionate-tris(pyrazole)methane with bulky substituents could cause sufficient elongation along the C_3 axis, due to steric hindrance, to reduce the quantum tunneling of magnetization (QTM) and increase the relaxation time to such an extent that SIM behavior would be observed at zero field.

Received 23rd July 2026,
Accepted 6th October 2026

DOI: 10.1039/d6dt01814a

rsc.li/dalton

Introduction

SMMs (Single-Molecule Magnets) are open-shell metal complexes exhibiting magnetic bistability at the molecular level and blockade of the magnetization below the so-called blocking temperature (T_B).[1–6] Because of this, these nanomagnets show slow relaxation of magnetization and magnetic hysteresis with remnant magnetization when the polarizing field is eliminated below T_B. These exceptional systems can show an appealing combination of the above indicated classical properties and quantum properties, such as quantum tunnelling of magnetization (QTM), quantum coherence, Berry phases, quantum oscillations and entanglement.[7,8] This combination of properties means that these materials could have potential applications in fields such as high-density information storage, quantum information processing using quantum states for designing qubits and qudits, quantum sensing, quantum simulation and molecular spintronics (spin-based electronics).[7–18] Over the last two decades, the field of SMMs has experienced a strong boost, mainly due to the achievements made with mononuclear Single-Molecule Magnets (MSMMs), also named Single-Ion Magnets (SIMs).[3–6,19–21] In these systems, the electronic structure and, therefore, the magnetic anisotropy can be deliberately regulated by playing with the features of the metal ion and ligands and the coordination sphere geometry, in other words by combining the action of spin–orbit coupling (SCO) and ligand field effects. The control

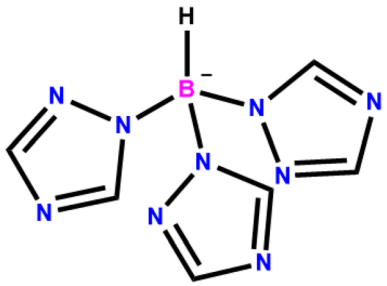
[a]Departamento de Química Inorgánica, Facultad de Ciencias, Universidad de Granada, 18071 Granada, Spain. E-mail: ecolacio@ugr.es, mpalacios@ugr.es
[b]National High Magnetic Field Laboratory, Florida State University, Tallahassee, Florida 32310, USA
[c]Departamento de Química Física y Química Analítica, Universidad de Jaén, Campus Las Lagunillas, s/n, 23071 Jaén, Spain

of the electronic structure allows the design of SIMs exhibiting large easy-axis magnetic anisotropy with marginal rhombicity; the main requirement to observe efficient SIM behaviour at zero magnetic field.[19–22] It is worth noting that Dy^{III}-based complexes generally exhibit the best MSMM properties, mainly due to strong magnetic anisotropy and the Kramers nature of the Dy^{III} ion.[23] In these systems, the joint action of a strong axial crystal field and very weak equatorial components minimizes the transverse magnetic anisotropy, thus favouring a strong easy-axis anisotropy and an outstanding MSMM behaviour.[19–22] This strategy has made it possible to obtain highly efficient Dy^{III} SIMs with large easy-axis anisotropy and the effective energy barrier for magnetization reversal (U_{eff}) and blocking temperature (T_B) as high as 1843 cm^{-1} and 100 K, respectively.[24–26] It should be noted that some multifunctional materials have recently been developed that combine efficient MSMM behaviour with properties such as chirality, luminescence, and circularly polarised luminescence (CPL), among others. These new multifunctional materials will undoubtedly open the door to new and sophisticated applications.[27–32]

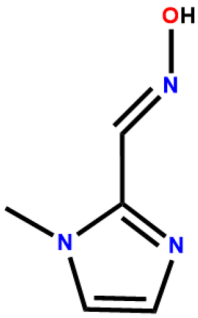
Among 3d-based MSMMs, those containing high-spin Co^{II} metal ions have also been extensively investigated[33–37] because of the following motivations: (i) in certain geometries, the Co^{II} complexes exhibit large values of the orbital angular momentum, and, as a result, strong first-order spin–orbit coupling (SOC) and magnetic anisotropy, (ii) when first-order SOC does not exist due to the action of a low-symmetry crystal field, strong anisotropy can emerge from second-order SOC, (iii) Co^{II} is a Kramers ion, so fast direct and QTM relaxation processes are not working at zero magnetic field, thus, in principle, favouring slow magnetic relaxation through Orbach and/or Raman thermally dependent processes, and (iv) strong easy-axis magnetic anisotropy, which is a crucial factor for observing MSMM behaviour at zero-field, can be achieved by molecular design. It is worth mentioning that mononuclear Co^{II} complexes with large easy-axis magnetic anisotropy are relatively infrequent and exhibit coordination numbers ranging from two to eight and a variety of geometries. Among them, the linear two-coordinate carbene complexes [(NHC)Co(Ndmp)][38] (NHC = N-heterocyclic carbene; dmp = dimesitylphenyl) and $[Co(C(SiMe_2ONaph)_3)_2]$[39] (where Me is methyl and Naph is a naphthyl group) have shown the best zero-field MSMM properties, with U_{eff} values larger than 400 cm^{-1} and open hysteresis up to 5 K. Mononuclear Co^{II} systems with trigonal planar, square pyramidal, trigonal bipyramidal, distorted pentagonal bipyramidal and square-antiprismatic geometries present moderate values of anisotropy and, as far as we are aware, almost none of them show significant slow relaxation at zero field, mainly due to strong Quantum Tunneling of Magnetization (QTM).[33–37] However, four-coordinate tetrahedral elongated Co^{II} complexes with approximate D_{2d} symmetry,[40–44] five-coordinate square-pyramidal complexes[45] and six-coordinate Co^{II} complexes with CoN_6 and CoO_6 trigonal prismatic[46–58] and antiprismatic coordination spheres[59–65] can also show large easy-axis magnetic anisotropy, with D (axial zero-field splitting parameter) values above −100 cm^{-1} and almost negligible E (rhombic zero-field splitting parameter) values. The elongated tetrahedral and trigonal prismatic complexes generally exhibit slow magnetic relaxation at zero-field or after magnetic dilution with maxima in the χ''_M *vs.* T plot even beyond 20 K and butterfly shaped hysteresis, which in a few cases is open at zero field at very low temperature. It is worth mentioning that only a few examples of fully magneto-structurally characterized trigonal antiprismatic complexes have been reported so far. Most of them have been prepared using scorpionate type tridentate ligands, such as hydridotris(pyrazole) borate, tetra(pyrazol)borate, tris(pyrazolyl)phosphine oxide and tris(pyrazolyl)methane derivatives.[59–65] Moreover, a series of Co^{III}–Co^{II}–Co^{III} salts have been reported, prepared by the reaction between a previously reported tris-chelate-type C_3 symmetric Co^{II}–metalloligand and Co^{II}.[63] The central Co^{II} center in these mixed-valence complexes exhibits a trigonal antiprismatic CoO_6 geometry (an octahedron elongated along the C_3 axis). Finally, the mixed-valence complexes $[Co^{II}Co^{III}_2(\mu\text{-}L^1)_2(Ph)_2(\mu\text{-}Cl)_2]\cdot DMF\cdot H_2O$, where HL^1 is *N*,*N*′-ethylenebis(salicylaldimine) and $[Co^{II}Co^{III}_2(L^2)_2\ (L^3)_2(CO_2CH_3)_2]$, where L^2 = (*R*) or (*S*)-2,4-di-*tert*-butyl-6-(4-hydroxo-3-phenylbut-1-en-1-yl)phenolate and L^3 = (*R*) or (*S*) 2-phenylglycinolate, have also been reported. These complexes were obtained by self-assembly of the ligands and the respective Co^{II} salts (chloride and acetate, respectively) and exhibit a rather distorted trigonal antiprismatic geometry.[64,65] Interestingly, despite the large strong easy-axis anisotropy of the Co^{II} ion in these compounds, none of them exhibited an out-of-phase (χ'') response under a zero dc magnetic field. In the presence of a small magnetic field, all these compounds present slow magnetic relaxation through Raman and QTM mechanisms.

We report here the synthesis, structures and magnetic properties of two additional examples of trigonal antiprismatic Co^{II} complexes. The first one is a neutral complex of the formula $[Co(Ttz)_2]$ that was obtained with the scorpionate ligand hydridotris(1,2,4-triazolyl)borate (Ttz^-), whereas the second one of the formula $[Co_3(L)_6](NO_3)_2\cdot 6H_2O$ is a mixed-valence Co^{III}–Co^{II}–Co^{III} trinuclear complex of C_3 symmetry prepared by self-assembly of the ligand 1-methylimidazole-2-carboxamide oxime (HL) and Co^{II} ions (see Scheme 1). The aim of this work is fourfold: (i) to confirm that these compounds present a strong easy-axis magnetic anisotropy in the Kramers ground state, (ii) to verify that, despite their strong easy-axis anisotropy, these compounds do not show slow magnetic relaxation at zero-field due to large QTM, (iii) to demonstrate experimentally and theoretically that the origin of the inherent QTM observed for these compounds is tied to their relatively large intrinsic transversal anisotropy and (iv) to disclose the magnetic relaxation mechanism for these compounds in the presence of a magnetic field and to analyse if a correlation exists between the axiality (g_{xy}/g_z) and the relaxation times extracted in the presence of dc magnetic fields for trigonal antiprismatic Co^{II} complexes. Finally, it should be noted in this regard that several experimental and theoretical magneto-structural correlations have recently been published for dis-

 This journal is © The Royal Society of Chemistry 2026



Ttz



HL

Scheme 1 Structures of the ligands.

torted Co^{II} tetrahedral complexes, showing that by modifying the ligands surrounding the Co^{II} ions and the substituents of those ligands, it is possible to modulate the values of D and E/D.[42–44] These studies demonstrate that the absence of a pure ground state and, furthermore, a higher E/D ratio, together with the concomitant reduction in axiality (g_{xy}/g_z), effectively triggers QTM. This is of great importance, since controlling axiality offers a way to reduce QTM and increase the relaxation time.

Experimental

Synthetic procedures

General procedures. All reactions were conducted in oven-dried glassware under aerobic conditions, and the analytical reagents were purchased from commercial sources and used without further purification.

Synthesis of sodium hydridotris (1,2,4-triazol-1-yl)borate (NaTtz)

1,2,4-Triazole (1 g, 14.5 mmol) and sodium borohydride (0.157 g, 4.14 mmol) were mixed in a round-bottom flask and heated to 90 °C. After 30 minutes, the temperature was increased to 120 °C and the mixture of the two solids melted. Then, the temperature was again increased to 185 °C and kept constant for 24 h. After this time, the temperature was allowed to decrease to 80 °C and the formed solid was washed two times with hot ethanol, two times with THF and dried under vacuum. Yield: 47%. Anal. calc. $C_6H_7N_9BNa$: C, 30.13; H, 2.93; N, 52.73. Found: C, 30.45; H, 3.05; N, 52.66. IR (cm^{-1}): 1500–1400, ν(C═N); 1271 ν(B–C) and 1182, 1145, δ(C–H). ^{1}H NMR (DMSO-d_6, ppm): 8.12 (s, H_{tz}), 7.83 (s, H_{tz}).

Synthesis of the ligand 1-methylimidazole-2-carboxamide oxime (HL)

To a methanolic solution (40 mL) of 1-methylimidazole-2-carbaldehyde (0.316 g, 4.54 mmol) were added hydroxylamine hydrochloride (0.5 g, 4.54 mmol) and sodium hydrogen carbonate (0.381 g, 4.54 mmol) and the mixture was refluxed overnight. The resulting solution was evaporated to dryness and the formed solid was dissolved in acetone. This solution was then filtered and evaporated to dryness to obtain the desired pale orange solid. Yield: 48%. Anal. calc. for $C_5H_7N_3O$: C, 48.00; H, 5.60; N, 33.60. Found: C, 48.12; H, 5.48; N, 33.80. IR (cm^{-1}): 3000, ν(CH); 1551–1419, ν(C═N and C═C) and 1160, δ(C–H). ^{1}H NMR (DMSO-d_6, ppm): 11.47 (s, H_{Oxime}), 8.05 (s, H_{imine}), 7.26 (d, $H_{imidazole}$), 6.98 (d, $H_{imidazole}$), 3.81 (s, H_{methyl}).

Synthesis of $[Co(Ttz)_2]_2{\cdot}5.5H_2O$ (1)

To a water solution of NaTtz (0.05 g, 0.23 mmol) was added a water solution of $CoCl_2{\cdot}6H_2O$ (0.027 g, 0.115 mmol) and the resulting amber solution was stirred for 15 minutes, filtered and kept at room temperature. After a few days, suitable pale yellow X-ray crystals were obtained by slow evaporation of the mother solution. Yield: 30%. Anal. calc. for $C_{24}H_{39}B_4Co_2N_{36}O_{5.5}$: C, 26.67; H, 3.63; N, 46.65. Found: C, 26.54; H, 4.01; N, 46.80. IR (cm^{-1}): 3093, ν(OH); 1504–1412, ν(C═N); 1292 ν(B–C) and 1197, 1146, δ(C–H). ESI-MS (Da): *m*/*z* 492.12, $[Co(Tzt)_2H]^+$; *m*/*z* 275.02, $[Co(Tzt)]^+$; *m*/*z* 766.14, $[Co(Tzt)_2] + [Co(Tzt)]^+$.

Synthesis of $[Co_3(L)_6](NO_3)_2{\cdot}6H_2O$ (2)

To a solution of 1-methylimidazole-2-carboxamide oxime ligand (0.05 g, 0.4 mmol) in 20 mL of ethanol was added sodium hydrogen carbonate (0.034 g, 0.4 mmol). Then, an ethanolic solution (20 mL) of $Co(NO_3)_2{\cdot}6H_2O$ (0.116 g, 0.4 mmol) was added dropwise and the resulting solution was stirred for 30 minutes and kept at room temperature. After several days, suitable X-ray crystals were obtained by slow diffusion of isopropanol into the mother solution. Yield: 11%. Anal. calc. for $C_{30}H_{48}Co_3N_{20}O_{18}$: C, 31.23; H, 4.19; N, 24.28. Found: C, 31.66; H, 4.11; N, 24.32. IR (cm^{-1}): 1578–1463, ν(C═N and C═C) and 1136, δ(C–H).

Physical measurements

Elemental analyses were performed on a Fisons-Carlo Erba analyser model EA 1108 and ^{1}H-NMR spectra were obtained on a 400 Hz "VARIAN DIRECT DRIVE" spectrometer at the "Centro de Instrumentación Científica" (University of

Granada). IR spectra were recorded on a Bruker Tensor 27 spectrophotometer by ATR detection. X-ray powder diffraction (XRPD) spectra were recorded on a (2θ) Bruker D2-PHASE using CuKα (λ = 1.5418 Å) radiation and the LINXEYE detector, from 5 to 50° (2θ) at a scanning rate of 0.5° 2θ min^{-1}.

Variable-temperature (2–300 K) magnetic susceptibility measurements were carried out on polycrystalline samples of compounds **1** and **2** under an applied field of 1000 Oe using a Quantum Design SQUID MPMS XL-5 device. Alternating-current (ac) susceptibility measurements under a dc field of 0.24 T for **1** and 0.18 T for **2** in the temperature range 2–15 K were performed on a PPMS-9 physical measurement equipment in the 100–10 000 Hz frequency range, using an oscillating field H_{ac} = 10 Oe for low frequencies and H_{ac} = 3 Oe for high frequencies. The magnetic susceptibility values were corrected for the diamagnetism of the molecular constituents and sample holder.

Far-infrared magnetic spectroscopy (FIRMS, also known as frequency-domain THz EPR spectroscopy)[66] experiments of compounds **1** and **2** were performed at the National High Magnetic Field Laboratory using a Bruker Vertex 80v FT-IR spectrometer coupled with a 17 T vertical-bore superconducting magnet in a Voigt configuration (light propagation perpendicular to the external magnetic field). The experimental setup employs broad band terahertz radiation emitted by a mercury arc lamp. The radiation transmitted through the sample was detected by a composite silicon bolometer (Infrared Laboratories) mounted at the end of the quasioptical transmission line. Both the sample and bolometer were cooled with low-pressure helium gas to the temperature of 5 K. The intensity spectra of the microcrystalline powder sample (~2 mg) bonded by *n*-eicosane were recorded in the spectral region between 14 and 730 cm^{-1} (0.42–22 THz) with an instrumental resolution of 0.3 cm^{-1} (9 GHz). To discern the magnetic absorptions, the transmission spectrum at each magnetic field was divided by the reference spectrum, which is calculated as the average spectrum for all magnetic fields after removing outlier points at each frequency. Such normalized spectra are only sensitive to tiny transmission changes induced by the magnetic field and exclude a strong nonmagnetic contribution due to vibrational absorptions and an instrumental function. All data analysis routines were implemented by the in-house written MATLAB code based on the EPR simulation software package EasySpin.[67]

High-frequency and -field EPR (HFEPR) spectra of compounds **1** and **2** were recorded at the National High Magnetic Field Laboratory in the 4.5–10 K temperature range on polycrystalline samples (20–25 mg), using a homodyne spectrometer at the EMR facility associated with a 15/17-T superconducting magnet and a frequency range from 52 to 426 GHz.[68] Detection was provided with an InSb hot electron bolometer (QMC Ltd, Cardiff, UK). The magnetic field was modulated at 50 kHz for detection purposes. A Stanford Research Systems SR830 lock-in amplifier converted the modulated signal to dc voltage.

Single-crystal structure determination

Suitable crystals of **1** and **2** were mounted on a glass fibre and used for data collection. X-ray diffraction data were obtained at 100 K using a Bruker D8 Venture diffractometer (MoKα radiation, λ = 0.71073 Å) outfitted with a PHOTON 100 detector.

Unit-cell parameters were determined and refined on all observed reflections using APEX4 software.[69] Correction for Lorentz polarization and absorption were applied by the SAINT[70] and SADABS[71] programs, respectively.

The structures were solved using SHELXT-2018[72] and refined by the full-matrix least-squares method on F^2 using the SHELXL-2018[73] and OLEX2 programs.[74] All non-hydrogen atoms were refined anisotropically. Hydrogen atom positions were calculated and isotropically refined as riding models to their parent atoms.

In the case of compound **2**, the counteranions and solvent molecules were very disordered, and they could not be modelled as discrete atomic sites. Contributions to scattering due to these highly disordered counteranions and solvent molecules were removed using SOLVENT MASK of OLEX2. A solvent mask was calculated, and 990 electrons were found in a volume of 2619 A^3 in one void per unit cell. This is consistent with the presence of 0.33 [NO_3^-] and 1 [H_2O] per asymmetric unit which account for 971 electrons per unit cell. This improves the model and good convergence was obtained at the end of the structure refinement.

A summary of selected data collection and refinement parameters can be found from the SI (Table S1) and CCDC 2573916 and 2573917.

Computational methodology

Quantum-chemical calculations were carried out from the crystallographic structures using the cif files. The electronic structure and magnetic properties have been computed using state averaged complete active space self-consistent field calculations (SA-CASSCF (7,5)),[75] followed by the N-electron valence second-order perturbation theory (NEVPT2) method[76–78] with the def2-TZVPP basis set,[79–81] including the auxiliary basis sets for correlation and Coulomb fitting for all the atoms. All calculations were done with the ORCA 5.0.4 quantum chemistry program package.[82] Spin Hamiltonian parameters (D, E and g-tensor) were computed using the effective Hamiltonian S = 3/2. In this case, spin–orbit effects were included using the quasi-degenerate perturbation theory (QDPT).[83–87] The employed active space includes seven electrons in five 3d-orbitals of Co^{II} CAS (7,5). We have included all 10 states for the 2S + 1 = 4 (quartet) states arising from the 4F and 4P terms of Co^{II}, and all the 40 states for the respective 2S + 1 = 2 (duplet) states arising from the 2P, 2D (twice), 2F, 2G and 2H terms of the Co^{II} ion. ORCA produces two sets of results CASSCF and NEVPT2. The splitting of d-orbitals due to the ligand field has been computed with the *ab initio* ligand field theory (AILFT)[88] module implemented in the ORCA program package.[82]

Results and discussion

The reaction of the scorpionate ligand hydrotris(1,2,4-triazol-1-yl) borate (Ttz$^-$) with $CoCl_2{\cdot}6H_2O$ in 2 : 1 molar stoichiometry

 This journal is © The Royal Society of Chemistry 2026

and using water as the solvent led to the neutral mononuclear Co^{II} complex of the formula $[Co(Ttz)_2]_2{\cdot}5.5H_2O$ (**1**). On the other hand, the reaction of the 1-methylimidazole-2-carboxamide oxime ligand (HL), $NaHCO_3$ and $Co(NO_3)_2{\cdot}6H_2O$ in ethanol and molar ratio 1 : 1 : 1 gave rise to a mixed-valence trinuclear Co^{III}–Co^{II}–Co^{III} coordination compound of the formula $[Co_3(L)_6](NO_3)_2{\cdot}6H_2O$ (**2**). As in the formation of other mixed-valence $Co^{III}Co^{II}Co^{III}$ complexes, where the oxidized cobalt centers are subjected to a strong ligand field, the oxidation of the two Co^{II} to Co^{III} had to be achieved by atmospheric oxygen.[64,65,89] In this case, this oxidation is favored by the strong ligand field promoted by the six-nitrogen atoms coordinated to the external cobalt centers. It is worth noting that the $Co^{II}N_6$ coordination sphere of **1** and the $Co^{II}O_6$ coordination sphere of **2** both present a distorted trigonal antiprism geometry.

The complexes have been characterised by X-ray powder diffraction (XRPD) to confirm the homogeneity and purity of the polycrystalline samples. For compound **1**, the X-ray powder diffractogram does not fully match with that generated from the corresponding X-ray single-crystal structure, which could be due to the partial loss of crystallization solvent water molecules during the grinding of the crystals and recording of the XRPD diffractogram (Fig. S1, left). Nevertheless, the elemental analysis results and the mass spectrum support the sample purity (see the Experimental part). In the case of complex **2**, the experimental and theoretical X-ray diffractograms almost coincide exactly, thus indicating the purity of the bulk sample (Fig. S1, right).

X-ray photoelectron spectroscopy (XPS) was used to support the oxidation state of the Co ions (Co^{II} and Co^{III}) belonging to the trinuclear complex **2** (Fig. S2). We have also obtained the XPS spectrum of the related complex $[(Co^{II}L4)_2Co^{II}]$,[58] (H_3L4 is the N_3O_3 tripodal ligand derived from the condensation of the *cis*, *cis*-1,3,5-tiaminocyclohexane with salicylaldehyde) for comparative purposes (Fig. S3). Although the binding energy values are commonly used to determine the oxidation state of a chemical element, for 3d transition elements the spin–orbit splitting is generally more informative. It is worth noting that experimental and theoretical calculations have shown that the Co $2p_{1/2}$–Co $2p_{3/2}$ spin–orbit splitting depends on the unpaired d electrons of the metal ion. Thus, in the compound containing diamagnetic Co^{III} ions this splitting is close to 15 eV, whereas for paramagnetic high-spin Co^{II} complexes it is around 16 eV.[90] According to this, the XPS spectrum of the compound $[(Co^{II}L4)_2Co^{II}]$ shows a spin–orbit splitting of 15.9 eV, whereas for compound **2** this splitting is 15 eV, which would be in agreement with the Co^{III}/Co^{II} mixed-valence nature of this compound. In addition to this, it has also been reported that Co^{II} complexes can show significant broadening of the Co $2p_{3/2}$ line and a marked increase in the intensity of the satellite lines, whereas the diamagnetic Co^{III} complexes generally show narrower Co $2p_{3/2}$ and satellite suppression.[90] The XPS spectra of $[(Co^{II}L4)_2Co^{II}]$ and **2** present the above indicated features. The significant reduction of the intensities of the Co $2p_{3/2}$ satellites in **2** compared with those in the $[(Co^{II}L4)_2Co^{II}]$ complex is good supporting evidence of the contribution of low-spin Co^{III} ions in **2**.

Crystal structures

Complex **1** crystallizes in the monoclinic space group *C*2/*c* and the structure consists of two crystallographically independent neutral mononuclear molecules with five and a half crystallization water molecules. In one of the molecules, the Co1 ion lies on a C_2 axis perpendicular to the B···Co···B direction (A), whereas in the other one the Co2 ion is located on the inversion centre (B). Within the neutral mononuclear units, the Co^{II} ions are coordinated to six nitrogen atoms belonging to the triazole groups of two different Ttz^- ligands with Co–N bond distances in the range of 2.112(2)–2.139(2) Å for Co1 and 2.112 (2)–2.135(3) Å for Co2 (Fig. 1). The selected bond lengths and angles are listed in Table S2.

The CoN_6 coordination environments present a slightly distorted octahedral geometry, which has also been confirmed with the continuous shape measure (CShM) analyses[91] performed for the two Co^{II} ions with *S* values of 0.505 and 0.308 for Co1 and Co2, respectively (see Table S3). The mean s/*h* ratio (defined as the mean donor–donor distance across a

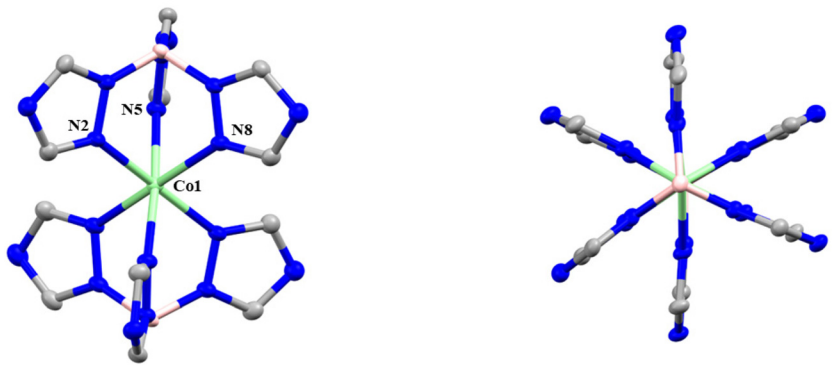


Fig. 1 ORTEP views of molecule A in the structure of **1** (left). Molecule A viewed along the pseudo-C_3 axis (right). Hydrogen atoms and crystallization water molecules are omitted for clarity. Color code: C grey, N blue, B pink, Co green.

triangular face divided by the donor–donor distances between the triangular parallel faces) is 1.22 for an ideal octahedron.[92] In the case of **1**, this parameter is 1.08 for Co1 and 1.09 for Co2, thus indicating a sizable elongation of the octahedron along the C_3 axis in both molecules. The distortion by trigonal compression or elongation can also be described by the α angle (angle between the Co···B line and each of the Co–N bonds). For $\alpha < 54.74°$, the octahedron is elongated along the pseudo C_3 axis, while for $\alpha > 54.74°$, it is compressed along this axis. For **1**, the α values are 51.58° for Co1 and 51.32° for Co2, which confirm that both Co1 and Co2 ions are in an N_6-elongated trigonal ligand field. Therefore, the CoN_6 coordination sphere of Co^{II} ions should be considered as an elongated trigonal antiprism with a symmetry close to D_3 and the C_3 axis lying along the B···Co···B direction. The two coordinated scorpionate ligands turn by about 60° (in the ranges 54.20°–63.61° and 58.08°–63.84° for units 1 and 2, respectively) to each other, giving rise to a paddle–wheel arrangement of the ligands when viewing the molecule along the pseudo-C_3 axis (Fig. 1, right). It is worth noting that the structural parameters for the two molecules of **1** are very similar to those previously reported for analogous complexes containing pyrazoyl instead of triazolyl groups.

Complex **1** exhibits intermolecular interactions between the nitrogen atom in the fourth position of two triazole groups of each ligand and crystallization water molecules with distances of 2.828 and 2.849 Å for Co1 and 2.784 and 2.899 Å for Co2. Moreover, there are hydrogen bond interactions between the crystallization water molecules with O···O distances in the range of 2.557–2.937 Å. The shortest Co^{II}···Co^{II} distances between neighbouring mononuclear units are established between the Co1 and Co2 ions with values of 7.893 Å and 7.950 Å, which indicate that the intermolecular dipolar interactions, if any, are very weak. Finally, the B–Co–B direction of the Co1-containing molecules is parallel to each other. A parallel disposition is also observed for the Co2-containing molecules. However, the B–Co–B directions of Co1- and Co2-containing molecules form an angle of 73.1° (Fig. S4).

Compound **2** crystallizes in the cubic system with the $Ia\bar{3}$ space group, and its structure consists of linear cationic Co^{III}–Co^{II}–Co^{III} trinuclear units, two nitrate anions for compensating charge and six crystallization water molecules (Fig. 2). The trinuclear cationic units belong to the S_6 point group, with the C_3 axis passing through the Co^{III}–Co^{II}–Co^{III} direction and the center of symmetry located at the central Co^{II} ion. Therefore, the Co^{III}–Co^{II}–Co^{III} are perfectly aligned forming an angle of 180.0°. The centrosymmetric cationic trinuclear entities are formed by the coordination of two *fac* trischelate $[Co^{III}(L)_3]$ units to the central Co^{II} ion through the oximate oxygen atoms of the ligands (Fig. 2).

The terminal Co^{III} ions present a distorted octahedral coordination geometry formed by three nitrogen atoms belonging to the imidazole groups and three nitrogen atoms belonging to the oximate groups. Within the $[Co^{III}(L)_3]$ units, the Co–$N_{imidazole}$ bond distance is 1.939(17) Å, while the Co–N_{oxime} bond distance is 1.924(15) Å. The central Co^{II} ion is coordinated by six oximate oxygen atoms with equal Co–O bond distances of 2.081(12) Å, leading to a trigonally distorted $Co^{II}O_6$ octahedral coordination geometry with local D_{3d} symmetry. The Co–N and Co–O distances are close to those expected for Co^{III} and high spin Co^{II} ions, respectively.[93] The oxidation states of the central and external cobalt centers were also confirmed by bond valence sum analysis (BVS). Thus, BVS for the central metal is 2.06, whereas BVS for the external ions is 3.13.[94,95] The inversion center on the central Co^{II} ion induces opposite chirality (Λ and Δ) on the two terminal Co^{III} and, therefore, the complex is achiral. Selected bond distances and angles for **2** are listed in Table S4.

The coordination geometry of the central Co^{II} ion has also been evaluated with continuous shape measurements using SHAPE software[91] ($S_{OC\text{-}6}$ = 0.012, see Table S3), thus confirming that the CoO_6 coordination sphere is very close to an ideal octahedral polyhedron. In this case, the mean s/*h* ratio is 1.26, indicating a small compression of the octahedron. The α angle of 55.40° is slightly larger than 54.74° (see above), thus confirming the small compression of the octahedron along the C_3 axis. Therefore, the CoO_6 coordination environment of the central Co^{II} ion can be considered as a compressed trigonal antiprism. The *fac* $[Co^{III}(L)_3]$ units are rotated relative to each

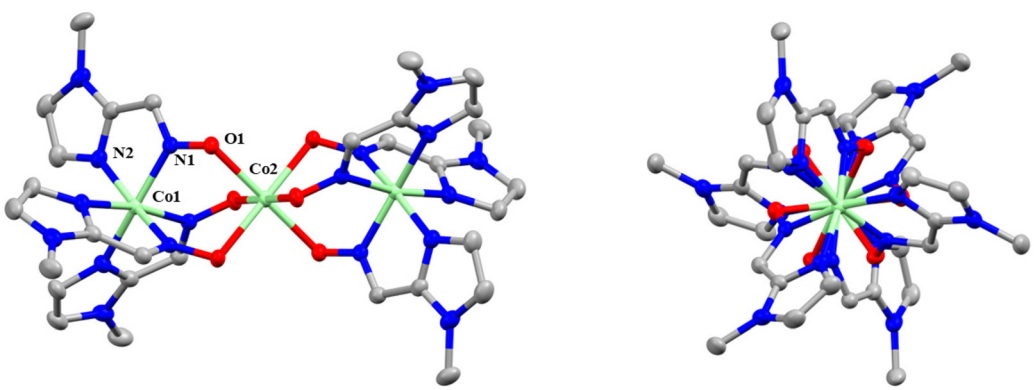


Fig. 2 ORTEP views of the molecular structure of **2**. The figure of the right panel corresponds to the molecule viewed along the C_3 axis. Hydrogen atoms, crystallization water molecules and anions are omitted for clarity. Color code: C grey, N blue, O red, Co green.

This journal is © The Royal Society of Chemistry 2026

other, giving rise, as in the case of **1**, to a paddle wheel arrangement of ligands. The Co^{III}–Co^{II} and Co^{III}–Co^{III} intramolecular distances are 3.479(13) Å and 6.958(3) Å, respectively, while the shortest intermolecular Co^{II}–Co^{II} interaction is 10.439 Å, just indicating that the trinuclear units are well isolated in the crystal structure. Finally, it is worth noting that, in the crystal packing, the C_3 axes of the trinuclear molecules are not parallel but form an angle of 70.53° with each other (Fig. S5).

Magnetic properties

The dc magnetic susceptibility of the polycrystalline samples of complexes **1** and **2** was recorded in the 2–300 K temperature range under an applied magnetic field of 1000 Oe and is given in the form $\chi_M T$ *vs.* T (χ_M being the molar magnetic susceptibility) in Fig. 3. The $\chi_M T$ values at room temperature for **1** and **2** are 2.88 and 2.78 $cm^3\ mol^{-1}$ K, respectively, which are much higher than the spin-only value for one isolated isotropic Co^{II} ion with $g = 2$ and $S = 3/2$ (1.875 $cm^3\ mol^{-1}$ K). This fact indicates a relevant orbital contribution of the Co^{II} ions. As the temperature is lowered, the $\chi_M T$ product of **1** and **2** almost remains constant until 130 K and then strongly decreases to reach values of 2.15 and 2.18 $cm^3\ mol^{-1}$ K at 2 K, respectively. This behavior is mainly due to the depopulation of the Kramers doublets arising from the spin–orbit coupling (SOC) effects, which ultimately are responsible for the magnetic anisotropy.

The field dependence of the isothermal magnetization for **1** and **2** in the 2–7 K temperature range and for magnetic fields ranging from 0 to 7 T is given in the insets of the left and right panels of Fig. 3, respectively. The magnetization values at 2 K and under the maximum applied field of 7 T for **1** and **2**, of 2.30$N\beta$ and 2.24$N\beta$, respectively, are significantly lower than the theoretical saturation value of 3$N\beta$ expected for an isolated Co^{II} ion with $g = 2$ and $S = 3/2$, which corroborates sizable magnetic anisotropy in these complexes. The M *vs.* H/T isotherms for compounds **1** and **2** (Fig. S6 and S7) show only a slight dependence on the temperature, thus suggesting that the energy separation between the ground and first excited Kramers doublets could be very large for these compounds, particularly for compound **2**, where the curves almost superimpose. Therefore, a strong magnetic anisotropy is expected for both compounds, although it is larger for **2**.

The dc magnetic data were analysed using a zero-field splitting spin Hamiltonian (hereafter named ZFS) and the Griffith–Figgis Hamiltonian (hereafter named GF).[96,97] The former does not consider first-order spin–orbit coupling, whereas the latter does. Although the use of the ZFS Hamiltonian in the case of **1** and **2** cannot be justified because of the strong first order spin–orbit orbital contribution expected for trigonal antiprismatic Co^{II} complexes, it has commonly been applied phenomenologically to study this type of complex.[60–65] For **1**, we have considered both units to be equal, although there are some minor differences between the D and E parameters calculated theoretically for these units (see Table 1).

The ZFS Hamiltonian is shown in eqn (1).

$$\hat{\boldsymbol{H}} = D\left[\hat{\boldsymbol{S}}_z^2 - S(S+1)/3\right] + E\left(\hat{S}_x^2 - \hat{S}_y^2\right) + \mu_B \sum_{i=x,yz} g_i \vec{H}_i \hat{\boldsymbol{S}}_i \quad (1)$$

where the first and second terms account for the axial magnetic anisotropy and the rhombic magnetic anisotropy, respectively, and the third term represents the Zeeman interaction. The susceptibility and magnetization data of **1** and **2** were simultaneously fitted using the PHI software[98] to the above Hamiltonian and considering an axial g matrix with $g_x = g_y$. Very good quality fits were obtained with the following parameters: $g_z = 2.845(2)$, $g_{xy} = 2.224(2)$, $D = -71.8(5)\ cm^{-1}$ and $|E| = 15.8(2)\ cm^{-1}$ and $R = 0.36 \times 10^{-3}$ for **1** and $g_z = 2.816(1)$, $g_{xy} = 2.125(1)$, $D = -82.5(2)\ cm^{-1}$ and $|E| = 14.4(2)\ cm^{-1}$ and $R = 0.35 \times 10^{-4}$ for **2** with $R = \left[\sum \left(M_{exp} - M_{calcd}\right)^2 \sum \left(\chi_{exp} - \chi_{calcd}\right)^2\right]$. The energy gap between the two lowest Kramers doublets is 153.7 cm^{-1} for **1** and 172.4 cm^{-1} for **2**. Interestingly, when the D parameter was forced to have positive values, the fit turned out to be of poorer quality, and, moreover, g_z and E parameters are unrealistic (see SI, table S5). However, almost identical values were obtained for E and for the quality of the fits when imposing positive or negative input values for this parameter. When E was fixed to zero, the other parameters slightly varied but the R value increased by one order of magnitude. It should be pointed out that the limitations of the

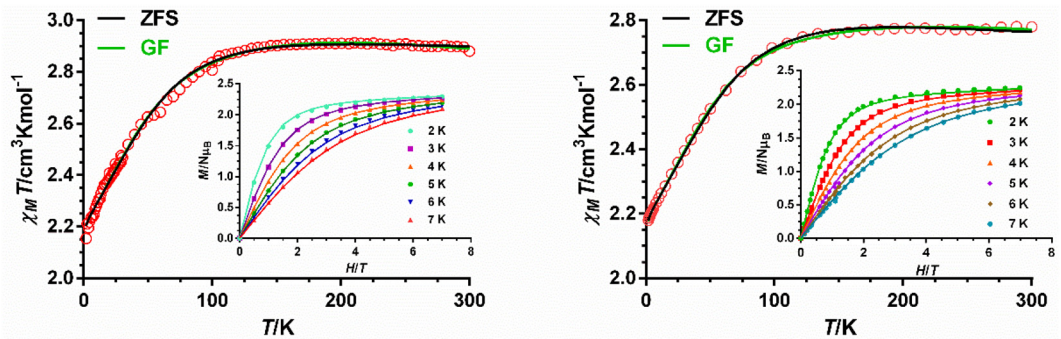


Fig. 3 Temperature dependence of $\chi_M T$ (red circles) and field dependence of the magnetization between 2 and 7 K (inset) for **1** (left) and **2** (right). Solid lines represent the best fit to eqn (1) (black line) and eqn (2) (green line) with the best-fit parameters.

Table 1 First excitation energies before and after including spin–orbit effects at the CASSCF + NEVPT2 level, together with the calculated D, E, g-tensors and effective g-tensors for the ground states of compounds **1** and **2**

Compound	Method	D (cm^{-1})	E/D	E (cm^{-1})	δE_1 (cm^{-1})	ΔE_1 (cm^{-1})	g_x, g_y, g_z [a] g'_x, g'_y, g'_z [b]
Compound **1**, unit 1	CASSCF/NEVPT2	−114.795	0.137784	−15.817	24.9	236.04	1.32, 1.47, 3.22[a] 0.89, 0.89, 8.88[b]
Compound **1**, unit 2	CASSCF/NEVPT2	−112.240	0.152433	−17.109	47.2	232.17	1.38, 1.56, 3.20[a] 0.97, 0.99, 8.79[b]
Compound **2**	CASSCF/NEVPT2	−112.083[c]	0.181520[c]	−20.345[c]	0.1	234.98	1.26, 1.45, 3.21[a] 1.18, 1.18, 8.71[b]

[a] g-Tensors for the true spin $S = 3/2$. [b] Effective g'-tensors assuming a pseudospin $S = 1/2$. [c] Obtained using the single_aniso module.

phenomenological approach based on the ZFS Hamiltonian for analysing complexes with first-order orbital contribution and the low accuracy of the magnetic measurements for determining the magnitude of D, and above all E and $|E/D|$ parameters, suggest that the ZFS parameters extracted for **1** and **2** may not be very reliable and should be treated with caution.

Given that complexes **1** and **2** are expected to exhibit significant unquenched orbital angular momentum, a GF Hamiltonian (eqn (2))[96] that explicitly takes into account this orbital contribution, would, in principle, be more appropriate than the ZFS Hamiltonian. The GF Hamiltonian is as follows:

$$\hat{H} = \sigma\lambda\hat{\boldsymbol{L}}\hat{\boldsymbol{S}} + \sigma^2 B_2^0\left(3\hat{\boldsymbol{L}}_z{}^2 - \hat{\boldsymbol{L}}^2\right) + \frac{B_2^2}{2}\sigma^2\left(\hat{\boldsymbol{L}}_x{}^2 - \hat{\boldsymbol{L}}_y{}^2\right) + \mu_B\left[-\sigma\hat{\boldsymbol{L}}_u + g_e\hat{\boldsymbol{S}}_u\right]\vec{H}_u(u = x, y, z) \quad (2)$$

The GF model uses the T–P isomorphism, which considers that the actual orbital angular momentum for the $^4T_{1g}$ ground state of the Co^{II} ion in an ideal Oh geometry is equal to the orbital angular momentum of the ^4P free ion term multiplied by −3/2 and therefore, $^4T_{1g}$ is considered as having an effective orbital moment $L_{eff} = 1$. The first term describes the interaction between the spin ($S = 3/2$) and orbital ($L = 1$) angular momenta *via* the spin–orbit coupling (SOC), where λ represents the SOC constant. The parameter σ is a combined reduction factor, which comprises the isomorphism coefficient (−3/2) and the orbital-reduction parameter (κ) that accounts for the covalence effect and the mixing of the $^4T_{1g}$ (^4F) and $^4T_{1g}$ (^4P) terms. As $0 < \kappa \leq 1$, then $0 > \sigma \geq -3/2$, although the usual values are found between −1.0 and −1.5.[97] The second and third terms represent the effect of the axial and rhombic crystal fields (B_2^0 and B_2^2 are the axial and rhombic crystal field parameters, respectively). Although the GF model was developed for octahedral or distorted octahedral complexes along the C_4 axis (whose ground term is either $^4T_{1g}$ (^4F) or derives from it, respectively), it has also been successfully applied to other geometries,[99,100] including those having a ground term of type ^4E (trigonal prismatic and antiprismatic Co^{II} complexes),[48,56,58,62,64] where the use of this model would be more doubtful. The $\chi_M T$ *vs.* T and M *vs.* H data were simultaneously fitted using PHI with the GF Hamiltonian. The best fits led to the following parameters: $B_2^0 = -276(2)$, $|B_2^2| = -62(1)$, $\lambda = 130.9(8)$ cm^{-1} and $\sigma = -1.46(3)$ for **1** and $B_2^0 = -558(1)$, $|B_2^2| = -101.8(1)$, $\lambda = 160.8(3)$ cm^{-1} and $\sigma = -1.433(2)$ for **2**. The energy gap between the two lowest energy levels is 152.2 cm^{-1} for **1** and 162.8 cm^{-1} for **2**. The Δ_{ax} and Δ_{rh} parameters, which represent the splitting of the $^4T_{1g}$ (F) ground term due to the axial and rhombic components of the crystal field, respectively, can be calculated from the extracted B_2^0 and B_2^2 parameters. The resulting values are $\Delta_{ax} = 1764(2)$ cm^{-1} and $\Delta_{rh} = 66(1)$ cm^{-1} for **1** and $\Delta_{ax} = 3437(1)$ cm^{-1} and $\Delta_{rh} = 104.5(1)$ cm^{-1} for **2**. As in the case of the magnetic parameters extracted using the ZFS Hamiltonian, when the input value of $B_2^0(\Delta_{ax})$ is positive the quality of the fitting with the GF Hamiltonian becomes poorer. However, the quality of the fit does not change when the input values of $B_2^2(\Delta_{rh})$ are positive or negative. Good fits are also obtained using values of B_2^2 close to zero, but the R value is one order of magnitude higher. Given that, as far as we know, there is no specific model for trigonal antiprismatic Co^{II} complexes accounting for the unquenched orbital angular momentum, the magnetic anisotropy parameters extracted also from the GF Hamiltonian should be treated with caution.

The analysis of the dc magnetic data clearly shows that, irrespective of the used Hamiltonian, compounds **1** and **2** show strong easy-axis magnetic anisotropy with non-negligible transverse anisotropy.

HFEPR and FIRM spectroscopies

To support the magnitude and sign of the magnetic anisotropy extracted from dc magnetic data, we recorded HFEPR and FIRM spectra. The HFEPR spectrum of **1** shows at low frequencies (58–141 GHz) two resonances, with effective g values of ~7.9 and 1.0 (the spectrum at 66 Hz is given in Fig. S8). These resonances could be assigned to the parallel ($B \| z$) and perpendicular ($B \| x$, y) turning points, respectively, of the intra-Kramers transition from M_S $|-3/2\rangle$ to M_S $|+3/2\rangle$ within the ±3/2 manifold. Although this transition is formally forbidden by the selection rule (for it $\Delta M_S = \pm 3$ and only transitions with $\Delta M_S = \pm 1$ are allowed), it can be observed because the selection rule is relaxed in the presence of the E-term in the zfs spin Hamiltonian. This rhombic anisotropy mixes the $|\pm 3/2\rangle$ and $|\pm 1/2\rangle$ Kramers doublets, so that the $|-3/2\rangle$ to $|+3/2\rangle$ transition becomes more allowed as E is larger. It is worth mentioning that the large g_z value observed in the spectrum is in the range usually found for Co^{II} complexes with strong easy-axis mag-

 This journal is © The Royal Society of Chemistry 2026

netic anisotropy.[47,58,101,102] Moreover, the observation of ($B\|x$, y) turning points in the spectrum suggests the existence of a significant rhombic anisotropy. In fact, the frequency *vs.* field dependence of both resonances (parallel and perpendicular, see Fig. S8) can only be reproduced (ignoring the intensities and considering the experimental D^* value of −102 cm^{-1} extracted from the FIRMs, see below) using the following zfs parameters: D = −99 cm^{-1}; E/D = 0.15, g = [2.18, 2.58, 2.67], which are close to those extracted from dc magnetic data. Unfortunately, no magnetic transitions could be observed in the 5–298 K and 58–141 GHz temperature and frequency ranges, respectively, for compound **2**. This fact cannot be explained by the rhombicity, which mixes the ground and first excited KDs, since E/D is similar but greater in **2** than in **1**. Fast magnetic relaxation in high-spin Co^{II} complexes can arise from spin-spin and spin-lattice relaxations. Since the intermolecular interactions, which favour magnetic relaxation, are weaker in **2** than in **1**, the relaxation in the former compound does not appear to be of spin-spin origin. However, the spin-lattice relaxation times, which are much shorter in compound **2** than **1**, as derived from ac susceptibility dynamic measurements (see below), could tentatively explain why the HFEPR spectrum for **2** is silent.

Although far-infrared magnetic spectroscopy (FIRMS) allows directly assessing the zero-field (zf) energy gap between the lowest-energy Kramers doublets (KDs) in an S = 3/2 spin system ($2D^*$), it does not provide any information on the rhombicity of the ZFS tensor for Kramers ions. The FIRMS heat map of compound **1** is shown in Fig. 4 together with the transmission spectra for 0 and 17 Tesla. Although large field-induced changes in the transmission are observed for this compound, the D^* value cannot be accurately extracted, because the spectra are affected by strong spin-phonon coupling effects (the ground state is vibronic, crystal field + phonon). As a result, the zero-field splitting (ZFS) energy is estimated to be approximately 203.7 ± 1 cm^{-1}. Regarding **2**, the heat map showed a very weak magnetic absorption feature near 210 cm^{-1}, which could correspond with the $2D^*$ value (Fig. S9). It is worth noting that the very weak and diffuse FIRMS response for **2** correlates with the silent HFEPR of this compound. So, it is feasible that the same mechanisms that are behind the FIRMs response are also the reason for the HFEPR resonance to be below the detection limit.

Theoretical calculations

We performed *ab initio* multiconfiguration calculations on the experimental X-ray crystal geometries of complexes **1** and **2**, using the ORCA 5.0.4 software package.[82] The calculated energies of the spin-free states (ligand-field terms) and those of the KDs generated by the spin–orbit (SO) coupling are given in Tables S6 and S7 for **1** and Tables S11 and S12 for **2**. The first excitation energies before and after including spin–orbit effects at the CASSCF and CASSCF + NEVPT2 levels, together with the calculated g-tensors and effective g-tensors, are shown in Tables S8 and S13 for **1** and **2**, respectively, whereas the CASSCF + NEVPT2 results are shown separately in Table 1. The orientation of the components of the g-tensor is shown in Fig. S10 for **1** and Fig. S13 for **2**.

The calculated spin-free state energies for **1** (Table S6) and **2** (Table S11) indicate that the energy gap between the ground and first excited states is very small (24.9 and 47.2 cm^{-1} for the units 1 and 2 of **1**, respectively, and 0.1 cm^{-1} for **2**), whereas the second excited state is located at almost 2000 cm^{-1} above the ground state. Therefore, the two lowest terms are almost degenerate in **1** and strictly degenerate by symmetry in **2** (the gap of 0.1 cm^{-1} between them can be considered an inherent error of the computational method), as expected for trigonal antiprismatic Co^{II} complexes with a ^{4}E ground term.

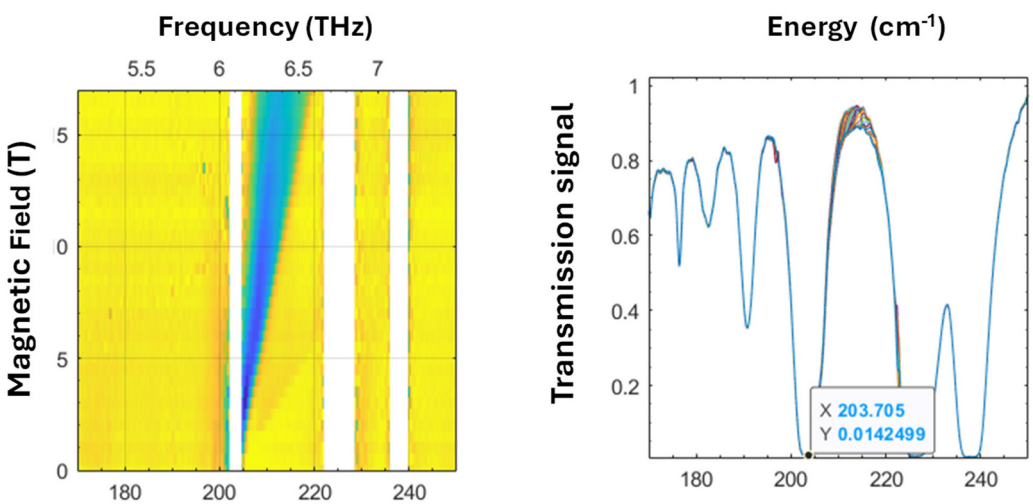


Fig. 4 (Left) Experimental 2-D (magnetic field *vs.* energy) heat maps of FIRMS response for complex **1**. Regions marked in blue represent resonance absorption that is sensitive to the changing magnetic field. Regions in yellow are insensitive to the field. The blank areas are those in which the sample was not transparent for far-infrared radiation. (Right) Transmission spectra recorded on the powder pellet of the complex at T = 4.2 K and at the indicated magnetic fields. The value of x in the inserted box indicates the value of $2D^*$.

Therefore, the Jahn–Teller distortion should be small and consequently the first-order orbital contribution very significant. In view of this, a strong SOC is anticipated, leading to the splitting of the ^{4}E term into four almost equidistant KDs with an energy gap between them of about 250 cm^{-1} (Tables S7 and S12). In view of the above considerations and the fact that the energy gap between the two lowest spin-free terms (Table S6) is much smaller than the energy separation between the two lowest KDs, it is reasonable to consider that the zfs would not be suitable for describing the electronic structure of complexes **1** and **2**. However, the fact that the energy separation between the ground and second excited KDs is about 500 cm^{-1} indicates that the population of the latter KD at 300 K is smaller than 5%. Under these conditions, the effective ZFS spin Hamiltonian (eqn (1)) could be phenomenologically used to provide a reasonable estimation of D and E anisotropy parameters. In the case of **2**, these parameters were calculated using the SINGLE_ANISO module in ORCA because for degenerate terms the perturbation theory diverges. As can be seen in Table 1, the values of the D and E parameters calculated for **1** and **2** are not far from those extracted from the magnetic data and, particularly, from FIRMS. However, as usual, the calculated parameters are greater, which may be due to the limitations inherent in both the calculation methods and the ZFS Hamiltonian-based approach. It is worth noting that the large effective g_z values ($g \sim 9$) calculated for **1** and **2** support the easy-axis anisotropy of the ground state, with the main anisotropy axis lying close to the B–Co–B and Co^{III}–Co^{II}–Co^{III} directions, respectively (Fig. S10 and S13, for **1** and **2**, respectively). Moreover, the effective g values indicate that the ground state is not pure Ising but mixed with excited states, thus favouring the QTM relaxation at zero field. In this regard, it should be indicated that the magnitude of the QTM depends on the tunnelling gap,[21,103] which in turn depends on the transversal magnetic moments. When the ground Kramers doublet is described with the effective spin $S_{eff} = \frac{1}{2}$, the transversal magnetic moments are related with the corresponding main values of the g factors, g_x, and g_y.[104] The axiality of the ground KD can then be measured from the g_{xy}/g_z ratio, so that the lower the value of this ratio is, the higher the axiality. Thus, the high axiality ($g_{xy}/g_z < 0.01$) is related to small values of the transversal magnetic moment and, therefore, weak QTM. However, in the case of compounds **1** and **2**, the theoretical CASSCF/NEVPT2 calculations show that the effective ground state g_x and g_y factors are not so small (0.87 and 0.98 for units 1 and 2 of **1**, respectively, and 1.18 for **2**), so that the g_{xy}/g_z ratio is one order of magnitude larger (0.1 for **1** and 0.14 for **2**), thus indicating that these compounds should present strong QTM. The g_{xy}/g_z values found for **1** and **2** are like those observed in other trigonal antiprismatic Co^{II} based field-induced MSMMs with easy-axis anisotropy (see Table 2).[59–65] Likewise, the absolute value of the transversal magnetic moment within the ground KD could also be used for measuring the strength of the QTM. For **1** and **2**, this value (0.30 and 0.33 for units 1 and 2 in **1**, respectively, and 0.39 for **2**, see Fig. S11 and S14) is larger than the generally assumed value of 0.1 necessary for an efficient relaxation mechanism *via* QTM and, therefore, strong QTM is expected for these compounds at zero applied magnetic field.

The splitting of the d-orbitals for complexes **1** and **2** was calculated using the *ab initio* ligand field (AILFT) method implemented in ORCA.[82] The computed energy diagrams for

Table 2 Structural and *ab initio* magnetic data for Co^{II} complexes exhibiting trigonal antiprismatic geometry and slow magnetic relaxation in the presence of a magnetic field

Compound	φ (°)	s/h	E/D	Effective g_x, g_y, g_z	Ref.
$[Co(Ttz)_2]_2{\cdot}5.5H_2O$ (**1**)	58.08, 54.20	1.085	0.138	0.89, 0.89, 888[a]	This work
	58.08, 62.32				
				0.97, 0.99, 8.78[b]	
	63.84, 63.61				
$[Co\{(O)P(O)(3,5\text{-}DMP)_2\}_2]$ (**10**)	52.80	1.01	0.27	1.51, 2.22, 7.67	62
	52.99				
	74.21				
$[Co(Tpm)_2][ClO_4]_2$ (**3**)	59.24	1.07	0.11	0.71, 0.73, 8.93	60
$[Co(Tpm)_2][BPh_4]{\cdot}2MeCN$ (**4**)	58.59	1.07	0.11	0.72, 0.74, 8.92	60
$[Co(Tp^*)_2]$ (**9**)	58.54	1.13		1.015, 1.041, 8.685[c]	61
$(Tp)_2Co$ monoclinic (**6**)	56.77	1.09	0.15	0.871, 0.892, 8.702	59
$(Tp)_2Co$ tetragonal (**7**)	59.40	1.11		0.998, 1.001, 8.747	59
$Tp_2Co{\cdot}2[(CH_3)_2NCS_2]_3Co$ (**5**)	59.34	1.12		0.848, 0.873, 8.801	59
$(pzTp^{Me})_2Co$ (**8**)	58.66	1.11		1.047, 1.059, 8.726	59
$[Co_3(L)_6]{\cdot}2NO_3^-{\cdot}6H_2O$ (**2**)	60	1.25	0.18	1.18, 1.18, 8.713	This work
$[Co_3(Himn)_6]\,Cl_2{\cdot}2CH_3OH$ (**11**)	60	0.84	0.14	0.94, 0.94, 9.10	63
$[Co_3(L)_2(Ph)_2(Cl)_2]{\cdot}(CH_3)_2CO{\cdot}H_2O$ (**12**)	55.29	0.96	0.32		64
	62.67				
	62.04				
$[Co_3(S\text{-}L1)_2(L2)_2(O_2CCH_3)_2]{\cdot}3(CH_3OH){\cdot}2(CH_2Cl_2)$ (**13**)	74.13	1.07	0.30		65
	26.67				
	79.21				

[a] Unit A. [b] Unit B. [c] CASPT2 calculations.

This journal is © The Royal Society of Chemistry 2026

these compounds are given in Fig. S12 for **1** and Fig. S15 for **2**, whereas the composition of the one-electron states appears in Tables S9 and S14, for **1** and **2**, respectively. The calculation results show that the splitting of the d orbitals is as expected for trigonal antiprismatic complexes (octahedral distorted along the C_3 axis). Thus, the lowest-lying d orbital is an essentially pure double-occupied d_{z^2}. At about 1400 cm^{-1} are located one doubly and one singly occupied d orbitals ($d_{x^2-y^2}$) and d_{xy} with some contributions of the d_{yz} and d_{xz} orbitals, respectively, which are almost degenerate in **1** and degenerate in **2**. Finally, at about 11 000 cm^{-1} the other two d orbitals are found, which are largely linear combinations of the d_{xz} and d_{yz} orbitals. These orbitals are also almost degenerate in **1** and degenerate in **2**. In both cases, the first excitation energy involves the transfer of a single electron from the higher doubly-occupied orbital (dominant d_{xy} character) to the first semioccupied orbital (dominant $d_{x^2-y^2}$ character), which are relatively close in energy (~100 cm^{-1} for **1** and degenerate in **2**) and have the same m_l value (±2). Therefore, the D value determined qualitatively from the spin allowed part of the second perturbative treatment[54,105] that depends on the inverse of the excitation energies should be very large and negative, which is in good agreement with the D values extracted from quantum chemical calculations and experimental magnetic data. It is worth mentioning that only the first quartet excited state is close/degenerate to the ground one (the second excited state is located at about 1800 cm^{-1} and at 1979 cm^{-1} above the ground state in **1** and **2**, respectively) and, therefore, the contribution to D essentially arises from the first excited spin-free quartet state for **1** (Table S10). In the case of **2**, as indicated elsewhere, the perturbation theory diverges and so this contribution to D and E could not be calculated.

Dynamic properties

In view of the large easy-axis magnetic anisotropy of **1** and **2**, we carried out temperature and frequency dependent ac magnetic susceptibility measurements with the aim of disclosing whether these compounds exhibit slow relaxation of magnetization. At zero field, neither **1** nor **2** present out-of-phase (χ''_M) signals, which can be due to the existence of sizable quantum tunnelling of magnetization (QTM), mainly promoted, as indicated by the theoretical calculations, by transverse anisotropy. Nevertheless, the contribution of intermolecular and hyperfine interactions cannot be ruled out. To try to eliminate the QTM and to determine the optimal dc field (that promoting the slowest magnetic relaxation), ac magnetic measurements were recorded in the presence of different magnetic fields (ranging from 0.02 T to 0.24 T) at very low temperature (6 K and 2 K for **1** and **2**, respectively). Under the applied magnetic fields, these compounds present frequency dependence of χ''_M (Fig. S16 and S17, left). The field dependence of the relaxation times was determined by fitting the frequency dependence of the out-of-phase signals to the generalized Debye model at each magnetic field. In the case of **1**, τ^{-1} values sharply decrease on increasing the magnetic field to 0.15 T, which is due to the attenuation of the QTM, and then they slightly decrease to reach an almost constant value of 0.24 T (Fig. S16 right). In view of this, the latter field was taken as the optimal field. For compound **2**, the τ^{-1} values decrease to 0.18 T, due to the gradual reduction of the QTM and then they slightly increase with the field due to the predominance of a direct relaxation process that is strongly field dependent. Thus, the field of 0.18 T was chosen as the optimal field (Fig. S17, right). The field dependence of the relaxation times at 6 K (**1**) or 2 K (**2**) was fitted to the following equation:

$$\tau^{-1} = AH^4T + B_1/1 + B_2H^2 + C \quad (3)$$

where the two first terms correspond to the field dependent direct and QTM relaxation processes, respectively, whereas the C constant represents the field independent relaxation processes (Raman and Orbach). The best fit allows extracting the parameters indicated in the right panels of Fig. S16 and S17.

A complete set of temperature- and frequency-dependent ac susceptibility measurements for **1** and **2** were then carried out at the corresponding optimal fields. Now, these compounds exhibit temperature and frequency dependence of the ac magnetic susceptibility (Fig. 5) with well-defined maxima in the range of 5.0 K (200 Hz)–11 K (10 000 Hz) for **1** and 2.5 K (200 Hz)–9 K (10 000 Hz) for **2**, just indicating that they behave as field-induced SIMs. In the case of **1**, under the optimal field, the QTM is not fully quenched, as evidenced by a small rising tail occurring below 5 K (Fig. S18). We tried to prepare the magnetically diluted compound (Co/Zn 1 : 10) with the aim of eliminating dipolar intermolecular interactions and, as a result, substantially reduce the QTM. However, all attempts to obtain the magnetically diluted compound were unsuccessful.

The Cole–Cole plots show semicircular shapes with small α values in the range of 0.029 (11 K)–0.064 (7 K) for **1** and 0.035 (9 K)–0.06 (4 K) for **2**, thus indicating the existence of a single relaxation process. Below 7 K for **1** and 4 K for **2**, α increases until reaching values of 0.29 (**1**) or 0.17 (**2**), due to the small QTM contribution at very low temperature (Fig. S19).

The relaxation times (τ) were obtained from the fitting of the frequency dependence of the ac χ''_M signals using the generalized Debye model (Fig. 5) and are given in the form τ^{-1} *vs.* T in the right panels of Fig. 5 and in the form $\ln\tau$ *vs.* $1/T$ in Fig. S20. The high temperature linear region of the temperature dependence of the relaxation times (Fig. S20) can be fitted to the Arrhenius law for a thermally activated relaxation process (Orbach process) with U_{eff} = 43.5 (7) K (30.25 cm^{-1}) and $\tau_0 = 3.5\ (1) \times 10^{-7}$ s for **1** and U_{eff} = 26 (1) K (17.82 cm^{-1}) and $\tau_0 = 1.4\ (1) \times 10^{-6}$ s for **2**. It should be noted that the extracted U_{eff} values are much lower than the experimental and calculated $|2D^*|$ values, which are above 200 cm^{-1}. In view of this, the Orbach relaxation process can be ruled out.

In view of this, the temperature dependence of τ^{-1} for **1** and **2** was fitted in the entirely studied temperature range using eqn (4).

$$\tau^{-1} = BT + {\tau_{QTM}}^{-1} + CT^n \quad (4)$$

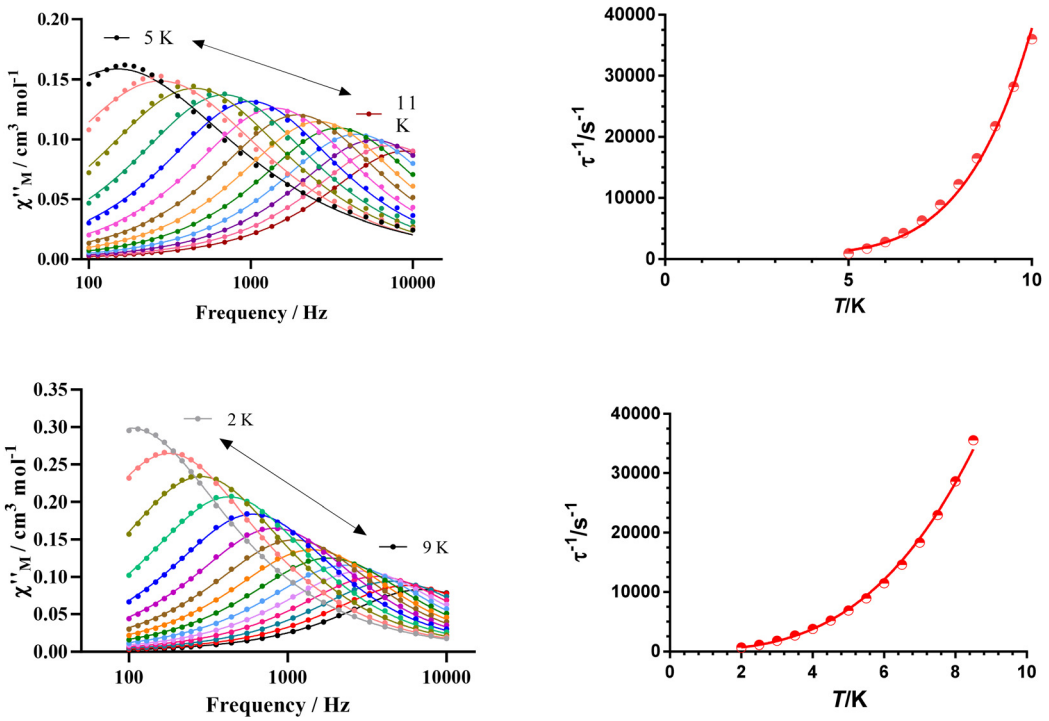


Fig. 5 (Top left) Frequency dependence of the χ''_M signals at different temperatures for **1** under a field of 0.24 T. The solid lines represent the best fitting to the Debye model. (Top right) Temperature dependence of τ^{-1} at 0.24 T for **1**. The solid line corresponds to the best fit to eqn (4). (Bottom left) Frequency dependence of the χ''_M signals at different temperatures for **2** under a field of 0.18 T. The solid lines represent the best fitting to the Debye model. (Bottom right). Temperature dependence of τ^{-1} at 0.18T for **1**. The solid line corresponds to the best fit to eqn (4).

where the first and second terms represent the field-dependent direct and QTM processes and the third term represents the field-independent Raman process. Although the Raman process is largely dominant, the direct and ${\tau_{QTM}}^{-1}$ relaxation processes must be considered to fit the data at low temperature. To avoid overparametrisation, the parameters corresponding to the direct (B) and ${\tau_{QTM}}^{-1}$ were fixed to the values extracted from the field dependence of the relaxation times (see Fig. S16 and S17). The best fit led to the following parameters: B = 26.7 s^{-1} K^{-1}, ${\tau_{QTM}}^{-1}$ = 132.9, C = 0.48 (4) s^{-1} K^{-n} and n = 4.9 (3) (R^2 = 0.9996), B = 68.8 s^{-1} K^{-1}, ${\tau_{QTM}}^{-1}$ = 110.2, C = 27.3 (5) s^{-1} K^{-n} and n = 3.3 (4) (R^2 = 0.9987) for **1** and **2**, respectively. Although for Kramers ions a n value of 9 is expected,[106,107] lower n values can be considered as acceptable depending on the structure of the levels, and if both, acoustic and optical phonons are considered.[106,107]

Because the spin relaxation can involve a vibrational excited state of the electronic ground state, the analysis of the τ^{-1} *vs.* T data was also carried out using the Raman mechanism through vibrational modes[108–111] that takes into consideration the contribution of the low energy optical phonons, instead of the T^n law (see Fig. S21). For it, we have used the following equation:

$$\tau^{-1} = D\frac{\exp\left(\frac{h\omega/2\pi}{k_B T}\right)}{\left[\exp\left(\frac{h\omega/2\pi}{k_B T}\right)-1\right]^2} + E\cot h(\delta/k_B T) \qquad (5)$$

where the small contribution from the QTM has been neglected. The first term corresponds to the Raman mechanism *via* the ω vibrational mode and the second term describes the direct mechanism between the states M_s = ±3/2. Under the corresponding optimal field, these states are not degenerate but are separated by an energy of $\delta/k_B T$. The best fit yielded vibrational modes with energies of 48.3 (9) cm^{-1} and 30 (1) cm^{-1} for **1** and **2**, respectively, which are not far from the low-energy vibrations observed in metal complexes. Therefore, regardless of the Raman mechanism (whether *via* vibrational modes or the power law), the Raman relaxation times decrease on moving from **1** to **2**.

Magneto-structural correlations

In Kramers type ions, like Co^{II}, the magnitude of the tunnelling gap (Δ_{tun}), which removes the double degeneracy of the KD and determines the strength of QTM (the rate of the QTM is nearly proportional to ${\Delta^2}_{tun}$),[21,112] is related to the product of the transversal transition magnetic moment within the Kramers doublets and the magnetic field in the system. This is because the Zeeman interaction of the transversal magnetic moments m_x and m_y and the related component of the magnetic field H_x and H_y are the sole responsible for inducing Δ_{tun}.[21,103,112] When $S_{eff} = \frac{1}{2}$ is used for describing the KD, the transversal magnetic moments depend on the main values of the effective g factors g_x and g_y. It is worth noting that the axiality of the KD can be determined by the g_{xy}/g_z ratio,[21,112] so

This journal is © The Royal Society of Chemistry 2026

that lower values of g_{xy}/g_z indicate higher axiality. In view of the above considerations, the larger the axiality, the smaller the transversal magnetic moment. Therefore, larger axiality leads to small strength of the QTM.

The experimental structural data and the *ab initio* calculated zfs and effective g_{ii} (x, y, z) parameters for Co^{II} complexes with a geometry close to trigonal antiprism (distorted octahedron along the C_3 axis) and ρ angles (rotation angle between the two parallel triangular faces located along the distortion pathway) close to 60° are given in Table 2. It is worth mentioning that, for comparative purposes, we have calculated the parameters for compounds **6** and **11** (see Tables S15 and S16) using the same computational method (CASSCF + NEVPT2 with ORCA 5.0.4). It is worth noting that the data extracted with the zfs Hamiltonian should be taken with caution because it may not be the most appropriate model for analyzing the electronic structure of these compounds with large orbital angular momentum.

The data collected in this table allow us to draw the following conclusions for this type of complex.

(1) When the donor atoms (D, either N or O) in the triangular faces that define the trigonal antiprismatic geometry are not of the same type, the D···D distances within the face and, consequently, the Co–D bond distances and D–Co–D bond angles can significatively differ in the Co^{II} coordination sphere, leading to an increase of the distortion. Thus, the axiality and E/D parameters calculated using *ab initio* methods decrease and increase, respectively, with the distortion. Examples of this type of system are complexes **10**, **12** and **13**. The first one is a mononuclear Co^{II} complex containing two tripodal scorpionate type ligands. Within each triangular face defining the trigonal antiprismatic geometry of this compound, there are two pyrazoyl nitrogen atoms and one oxygen atom belonging to a phosphine oxide ligand, all of them coordinated to the Co^{II} ion giving rise to a CoN_4O_2 coordination sphere. Compounds **12** and **13** are trinuclear Co^{III}–Co^{II}–Co^{III} complexes, where the magnetically active central Co^{II} ion is coordinated by four phenolato oxygen atoms and two chloride atoms in the former and by six oxygen atoms in the latter, all of them acting as bridging groups. As in **10**, the donor atoms within each face defining the $Co^{II}O_4Cl_2$ and $Co^{II}O_6$ trigonal antiprismatic geometries, respectively, are not equal. This is obvious in the former compound containing two phenolate and one chloride donor atoms, while in the latter one each trigonal face comprises two alkoxo and one acetate oxygen atoms. As can be observed in Table 2, the g_{eff} values for **10**, **12** and **13** point out a significant rhombic contribution to the axial anisotropy in these compounds.

(2) The rest of the compounds given in Table 2 present trigonal antiprismatic geometries with ρ angles close to 60° and equal donor atoms (oxygen or nitrogen) within the faces defining the trigonal antiprismatic geometry. All these compounds, either mononuclear or trinuclear, show easy-axis magnetic anisotropy ($g_z \gg g_{xy}$), and the axiality increases (and the E/D decreases) when the s/h ratio decreases, that is to say when the compounds are more elongated along the C_3 or pseudo C_3 axis (see Fig. 6 and Fig. S22). The small deviations regarding the expected elongation pathway can be due, among other reasons, to the small differences between the values of the ρ angles (see Table 2). This is because it has been demonstrated by *ab initio* calculations that when the ρ angle decreases from 60° the axiality increases (and E/D decreases). To confirm the effect of the distortion along the C_3 or pseudo-C_3 axis, we have performed *ab initio* calculations starting from compound **1**, maintaining the distances between the three nitrogen donor atoms within the triangular faces defining the trigonal antiprismatic geometry and moving the parallel planes of the donor atoms of these faces away from and toward the Co^{II} ion by 0.1 and 0.2 Å (Table S17). These shifts obviously change the Co–N and N–Co–N angles. As can be observed in Fig. 6, the dependence of the axiality on s/h is quasi-linear, increasing in the former cases and decreasing in the latter ones. The same trend is observed for the dependence of E/D on s/h, but the increase of E/D when the donor atoms of each ligand are moved toward the Co^{II} ion is more abrupt than when these atoms are moved away (Fig. S22). For compound **1**, the value of s/h for $g_{xy}/g_z = 0$ (maximum value of axiality) was estimated to be 0.55 from the equation of the straight line obtained by fitting the calculated axiality *vs.* s/h ($R = 0.99$). This s/h value would lead to Co–N distances of 2.46 Å, which seems to be very unrealistic. Therefore, in principle, this s/h could not be achieved, and this is the reason why the calculated g_{xy}/g_z values for the reported trigonal antiprismatic Co^{II} complexes are larger than 0.1 (see Table 2). It should be noted at this point that we have not used CShM values to correlate axiality with distortion of the octahedron along the C_3 axis to achieve a trigonal antiprismatic geometry, because they do not reflect that distortion as well as s/h does.

(3) The calculated values of the axial zfs parameter (D) for the compounds indicated in point 2 are very similar in sign and magnitude (≈−100 cm^{-1}) to those extracted for trigonal prismatic Co^{II} complexes exhibiting slow magnetic relaxation and SMM behaviour at zero applied magnetic field.[46–49,58]

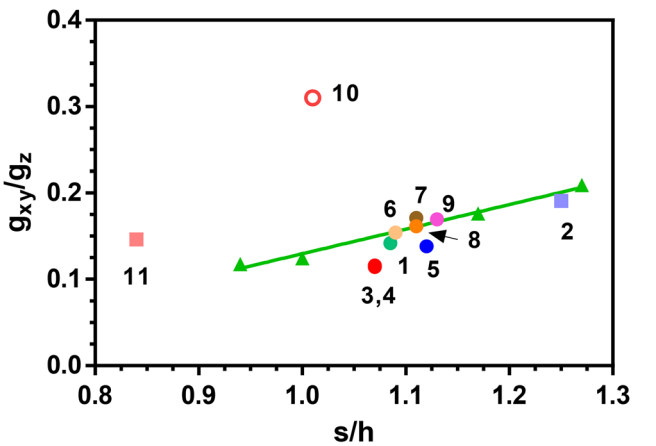


Fig. 6 Dependence of the *ab initio* axiality on the s/h parameter for the indicated trigonal antiprismatic Co^{II} complexes.

Considering this, one might wonder why trigonal antiprismatic Co^{II} complexes never show slow magnetic relaxation at zero field. The answer can be found in the values of axiality. Thus, while homoleptic trigonal prismatic Co^{II} complexes with very small ρ angles present calculated g_{xy}/g_z values close to zero and almost pure Ising anisotropy, trigonal antiprismatic homoleptic Co^{II} complexes exhibit calculated values of g_{xy}/g_z larger than 0.1. This inherent relatively high value of g_{xy}/g_z reduces the axiality and enables fast QTM, which hinder the SMM behaviour at zero-field. We have estimated the QTM relaxation times (τ_{QTM}^{-1}) for trigonal antiprismatic Co^{II} complexes from the *ab initio* calculated *g*-values, following the method recently proposed by Yin *et al.*[113–115]

$$\tau_{QTM}^{-1} = \frac{\beta B_{av}}{h} \frac{g_{xy}^2}{2\sqrt{g_{xy}^2 + g_z^2}} \qquad (6)$$
$$g_{xy}^2 = \sqrt{g_x^2 + g_y^2}$$

where B_{av} is the average strength of local magnetic fields around the ion (the local magnetic field is assumed to be isotropic). Since B_{av} is very difficult to be obtained by theoretical calculations, it is selected on the basis of previous information. In this regard, magnetic fields due to either electronic dipolar interactions or hyperfine interactions were reported to be of few tens of mT.[1,7] Therefore, the selection of B_{av} will give rise to the precision limit. We have used for the Co^{II} ion the value empirically employed for lanthanide ions of about 20 mT, which has shown to afford relaxation times consistent with the experimental ones at the order of magnitude level.[114] The extracted QTM relaxation times were: t_{QTM} = 5.1 x 10^{-8} s (unit 1 of **1**), t_{QTM} = 4.6 x 10^{-8} s (unit 2 of **1**) and t_{QTM} = 3.7 x 10^{-8} s (for **2**). The lack of rigorousness in the selection of Bav does that the extracted relaxation times can be considered as qualitative estimates. The QTM analysis illustrates that for trigonal antiprismatic complexes, which have axiality values larger than 0.1, the ground state transition is too fast for experimental observation of any slow relaxation at zero field (typical ac susceptibility measurements use frequencies from 0.1 to 10000 Hz or ca. 10 to 10^{-4} s). It should be noted that even if the selected B_{av} were found in the range of one order of magnitude around 20 mT (2 mT to 200 mT) the calculated relaxation times would be too fast to observe, using ac measurements, zero-field slow magnetic relaxation in these Co^{II} complexes.

(4) Using the Raman, direct and QTM parameters extracted from the fitting of the temperature dependence of τ^{-1} described by eqn (4) for trigonal antiprismatic complexes with calculated effective *g* values (see Fig. S23), we have presented in Fig. 7 the dependence of the relaxation times at 5 K (at this temperature the Raman will be the principal relaxation process) on the axiality (g_{xy}/g_z). The aim of this is to know if there is a relationship between these two magnitudes. As can be seen in Fig. 7, in general, the relaxation times steadily increase with increasing axiality (decreasing g_{xy}/g_z). Moreover, complexes containing neutral trispyrazoylmethano ligands (**3** and **4**), which lead to larger axiality, are those having a longer

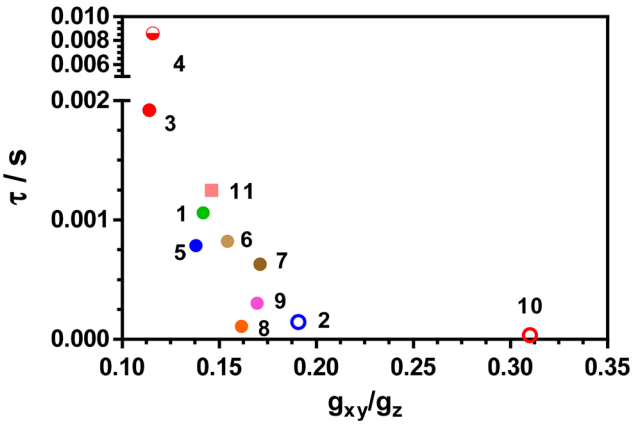


Fig. 7 Dependence of the relaxation time on the axiality for the indicated trigonal antiprismatic Co^{II} complexes at 5 K.

relaxation time, whereas the neutral compound **10**, possessing smaller axiality, due to a larger distortion of the geometry, exhibits the shortest relaxation time. Nevertheless, it is worth noting that compound **4** exhibits an abnormally higher value of relaxation than **3**, which was justified by the existence in the former of weaker dipolar interactions than in the latter due to the presence of larger size anions in **4** than in **3** (BPh_4^- *versus* ClO_4^- anions).[60] To prove if this hypothesis is correct, it should be necessary to prepare more examples of this kind of ionic compound, because the rest of the reported trigonal prismatic complexes are neutral and do not contain counteranions. The relaxation times for neutral compounds containing anionic trispyrazoil and tetrapyrazoyl borate complexes (the rest of the compounds except for **2** and **11**), as well as the neutral trinuclear Co^{II}–Co^{III}–Co^{II} complexes (**2** and **11**), which have an anionic metalloligand, are found between **4** and **10**, following the general trend. This fact indicates that the relaxation time is primarily affected by the axiality and not by the type of donor atom of the ligand (O for **2** and **11** and N for the rest). Finally, it is clear that the determination of accurate values of axiality and *E/D* ratio is of central importance for designing Co^{II} based SIMs with longer relaxation times. In this regard, a direct experimental determination of these parameters (g_{xy}/g_z and *E/D*) using torque magnetometry on square-pyramidal Co^{II} complexes has been recently reported.[45] The results of this study reproduce the experimental parameters extracted from magnetic data and theoretical calculations, thus demonstrating the reliability of this method.

Conclusions

We reported two cobalt complexes, a neutral mononuclear complex of the formula $[Co^{II}(Ttz)_2]_2 \cdot 5.5H_2O$ (**1**) and a mixed-valence Co^{III}–Co^{II}–Co^{III} trinuclear complex with C_3 symmetry and the formula $[Co_3(L)_6](NO_3)_2 \cdot 6H_2O$ (**2**). In the mononuclear complex, the Co^{II} ions exhibit an elongated trigonal antiprismatic coordination geometry, whereas in the trinuclear

This journal is © The Royal Society of Chemistry 2026

complex the coordination environment is a compressed trigonal antiprism. The dc magnetic properties, FIRMS measurements and theoretical calculations confirmed that both complexes show strong easy-axis magnetic anisotropy with non-negligible transverse anisotropy. Moreover, theoretical calculations predicted strong quantum tunneling of magnetization (QTM) for these compounds under zero applied magnetic field, which is experimentally confirmed by the absence of slow magnetic relaxation. However, under an optimal dc field, both complexes exhibit slow relaxation of magnetization through Raman, QTM and direct relaxation processes and therefore behave as field-induced single-ion magnets (SIMs).

The exhaustive experimental and theoretical magneto-structural studies carried out for all trigonal antiprismatic Co^{II} complexes reported so far, including **1** and **2**, allow the following conclusions to be drawn: (i) all trigonal antiprismatic complexes present easy-axis magnetic anisotropy with inherent significant transversal anisotropy ($g_{xy}/g_z > 0.1$), thus leading to very short relaxation times as to observe SMM behaviour at zero-field. (ii) Although improbable, the only possibility to observe this behaviour in trigonal antiprismatic complexes would be that of using scorpionate-tris(pyrazol)methane based neutral ligands, like that of **3** and **4**, with bulky substituents to favour the elongation of the Co^{II} coordination sphere along the C_3 axis, and large anions to separate the trigonal antiprismatic CoN_6 units decreasing the dipolar interactions. All these factors could reduce the QTM and increase the relaxation time to such an extent as to observe SMM at zero-field. Work along this line is in progress in our group.

Conflicts of interest

There are no conflicts of interest to declare.

Data availability

The data supporting this article have been included as part of the supplementary information (SI). Supplementary information: crystallographic data, PXRD, XPS spectra, magnetic plots and tables, and computational analysis plots and tables. See DOI: https://doi.org/10.1039/d6dt01814a.

CCDC 2573916 and 2573917 contain the supplementary crystallographic data for this paper.[116a,b]

Acknowledgements

Financial support from Ministerio de Ciencia e Innovación (Project PID2022-138090NB-C21 funded by MCIN/AEI/10.13039/501100011033/FEDER, UE), Consejería de Universidad, Investigación e Innovación and ERDF Andalusia Program 2021–2027 (projects C-EXP-140-UGR23 and M.1.B.B TA_000722_UJA23), Junta de Andalucía (FQM-195 and FQM-337), the University of Granada and the University of Jaén is gratefully acknowledged. M. M. Q. M. thanks Ministerio de Ciencia e Innovación for their Ramón y Cajal contracts (RYC2021-034288-I funded by MCIN/AEI/10.13039/501100011033 and by European Union "NextGenerationEU"/PRTR"). A portion of this work was performed at the National High Magnetic Field Laboratory, which is supported by the NSF (Cooperative Agreement No. DMR-2128556) and the State of Florida. The authors are grateful to Dr. V. K. Abdelkader from University of Granada for his help in XPS spectra analysis.

References

1 D. Gatteschi, R. Sessoli and J. Villain, *Molecular Nanomagnets*, Oxford University Press, Oxford, 2006.
2 Y.-S. Meng, S.-D. Jiang, B.-W. Wang and S. Gao, *Acc. Chem. Res.*, 2016, **49**, 2381–2389.
3 M. Feng and M. Tong, *Chem. – Eur. J.*, 2018, **24**, 7574–7594.
4 A. Zabala-Lekuona, J. M. Seco and E. Colacio, *Coord. Chem. Rev.*, 2021, **441**, 213984.
5 N. F. Chilton, *Annu. Rev. Mater. Res.*, 2022, **52**, 79–101.
6 X. Yin, L. Deng, L. Ruan, Y. Wu, F. Luo, G. Qin, X. Han and X. Zhang, *Materials*, 2023, **16**, 3568.
7 D. Gatteschi and R. Sessoli, *Angew. Chem., Int. Ed.*, 2003, **42**, 268–297.
8 E. Moreno-Pineda and W. Wernsdorfer, *Adv. Quantum Technol.*, 2024, **8**, 2300367.
9 G. Taran, E. Bonet and W. Wernsdorfer, in *Handbook of Magnetism and Magnetic Materials*, ed. J. M. D. Coey and S. S. P. Parkin, Springer International Publishing, Cham, 2021, pp. 979–1009.
10 L. Bogani and W. Wernsdorfer, *Nat. Mater.*, 2008, **7**, 179–186.
11 D. Gatteschi, A. Cornia, M. Mannini and R. Sessoli, *Inorg. Chem.*, 2009, **48**, 3408–3419.
12 R. Vincent, S. Klyatskaya, M. Ruben, W. Wernsdorfer and F. Balestro, *Nature*, 2012, **488**, 357–360.
13 E. Coronado, *Nat. Rev. Mater.*, 2019, **5**, 87–104.
14 E. Moreno-Pineda and W. Wernsdorfer, *Nat. Rev. Phys.*, 2021, **3**, 645–659.
15 B. R. Sankhi, E. Peigney, H. Brown, P. Suh, C. Rojas-Dotti, J. Martínez-Lillo and P. Tyagi, *J. Magn. Magn. Mater.*, 2024, **611**, 172608.
16 E. Moreno-Pineda, C. Godfrin, F. Balestro, W. Wernsdorfer and M. Ruben, *Chem. Soc. Rev.*, 2018, **47**, 501–513.
17 P. Kazmierczak, R. Mirzoyan and R. G. Hadt, *J. Am. Chem. Soc.*, 2021, **143**, 17305–17315.
18 C.-J. Yu, S. von Kugelgen, D. W. Laorenza and D. E. Freedman, *ACS Cent. Sci.*, 2021, **7**, 712–723.
19 J.-L. Liu, Y.-C. Chen and M.-L. Tong, *Chem. Soc. Rev.*, 2018, **47**, 2431–2453.
20 Y.-S. Meng, S.-D. Jiang, B.-W. Wang and S. Gao, *Acc. Chem. Res.*, 2016, **49**, 2381–2389.
21 L. Ungur and L. F. Chibotaru, *Inorg. Chem.*, 2016, **55**, 10043–10056.
22 Z. Zhu and J. Tang, *Natl. Sci. Rev.*, 2022, **9**, nwac194.

23 J. D. Rinehart and J. R. Long, *Chem. Sci.*, 2011, **2**, 2078–2085.
24 C. A. P. Goodwin, F. Ortu, D. Reta, N. F. Chilton and D. P. Mills, *Nature*, 2017, **548**, 439–442.
25 F.-S. Guo, B. M. Day, Y.-C. Chen, M.-L. Tong, A. Mansikkamäki and R. A. Layfield, *Science*, 2018, **362**, 1400–1403.
26 J. Emerson-King, G. K. Gransbury, B. E. Atkinson, W. J. A. Blackmore, G. F. S. Whitehead, N. F. Chilton and D. P. Mills, *Nature*, 2025, **643**, 125–129.
27 A. G. Bispo-Jr, *Coord. Chem. Rev.*, 2025, **537**, 216685.
28 Z. Zhu, C. Zhao, T. Feng, X. Liu, X. Ying, X.-L. Li, Y.-Q. Zhang and J. Tang, *J. Am. Chem. Soc.*, 2021, **143**, 10077–10082.
29 Z. Zhu, S. Paul, C. Zhao, J. Wu, X. Ying, L. Ungur, W. Wernsdorfer, F. Meyer and J. Tang, *J. Am. Chem. Soc.*, 2024, **146**, 18899–18904.
30 Z. Zhu, T. Wang, L. A. Mariano, S. Paul, W. Wernsdorfer, A. Lunghi and J. Tang, *J. Am. Chem. Soc.*, 2025, **147**, 42815–42824.
31 R. Rabelo, L. M. Toma, A. Bentama, S.-E. Stiriba, R. Ruiz-García and J. Cano, *Magnetochemistry*, 2024, **10**, 107.
32 B. El Rez, J. Liu, V. Béreau, C. Duhayon, Y. Horino, T. Suzuki, L. Coolen and J.-P. Sutter, *Inorg. Chem. Front.*, 2020, **7**, 4527–4534.
33 A. Sarkar, S. Dey and G. Rajaraman, *Chem. – Eur. J.*, 2020, **26**, 14036–14058.
34 J. Juráková and I. Šalitroš, *Monatsh. Chem.*, 2022, **153**, 1001–1036.
35 P. K. Sahu, R. Kharel, S. Shome, S. Goswami and S. Konar, *Coord. Chem. Rev.*, 2023, **475**, 214871.
36 M. Wang, Z. Han, Y. Garcia and P. Cheng, *ChemPhysChem*, 2024, **25**, e202400396.
37 A. Dey, S. Roy and S. Das, *CrystEngComm*, 2025, **27**, 7460–7483.
38 P. C. Bunting, M. Atanasov, E. Damgaard-Møller, M. Perfetti, I. Crassee, M. Orlita, J. Overgaard, J. van Slageren, F. Neese and J. R. Long, *Science*, 2018, **362**, eaat7319.
39 X.-N. Yao, J.-Z. Du, Y.-Q. Zhang, X.-B. Leng, M.-W. Yang, S.-D. Jiang, Z.-X. Wang, Z.-W. Ouyang, L. Deng, B.-W. Wang and S. Gao, *J. Am. Chem. Soc.*, 2017, **139**, 373–380.
40 M. S. Fataftah, J. M. Zadrozny, D. M. Rogers and D. E. Freedman, *Inorg. Chem.*, 2014, **53**, 10716–10721.
41 Y. Rechkemmer, F. D. Breitgoff, M. van der Meer, M. Atanasov, M. Hakl, M. Orlita, P. Neugebauer, F. Neese, B. Sarkar and J. van Slageren, *Nat. Commun.*, 2016, **7**, 10467.
42 S. Vaidya, S. Tewary, S. K. Singh, S. K. Langley, K. S. Murray, Y. Lan, W. Wernsdorfer, G. Rajaraman and M. Shanmugam, *Inorg. Chem.*, 2016, **55**, 9564–9578.
43 S. Vaidya, K.S. Singh, P. Shukla, K. Ansari, G. Rajaraman and M. Shanmugam, *Chem. Eur. J.*, 2017, **23**, 9546–9559.
44 S. Vaidya, P. Shukla, S. Tripathi, E. Rivière, T. Mallah, G. Rajaraman and M. Shanmugam, *Inorg. chem.*, 2018, **57**, 3371–3386.
45 V. Thangaraj, D. Sartini, D. Borah, D. Chauhan, V. Sharma, L. Sorace, G. Rajaraman, M. Perfetti and M. Shanmugam, *Adv. Sci.*, 2025, **12**, e2415624.
46 A. Landart-Gereka, M. M. Quesada-Moreno, M. A. Palacios, I. F. Díaz-Ortega, H. Nojiri, M. Ozerov, J. Krzystek and E. Colacio, *Chem. Commun.*, 2023, **59**, 952–955.
47 A. Landart-Gereka, M. M. Quesada-Moreno, I. F. Díaz-Ortega, H. Nojiri, M. Ozerov, J. Krzystek, M. A. Palacios and E. Colacio, *Inorg. Chem. Front.*, 2022, **9**, 2810–2831.
48 A. Landart, M. M. Quesada-Moreno, M. A. Palacios, Y. Li, M. Ozerov, J. Krzystek and E. Colacio, *Dalton Trans.*, 2024, **53**, 12876–12892.
49 A. A. Pavlov, D. Y. Aleshin, S. A. Savkina, A. S. Belov, N. N. Efimov, J. Nehrkorn, M. Ozerov, Y. Z. Voloshin, Y. V. Nelyubina and V. V. Novikov, *ChemPhysChem*, 2019, **20**, 1001–1005.
50 A. A. Pavlov, Y. V. Nelyubina, S. V. Kats, L. V. Penkova, N. N. Efimov, A. O. Dmitrienko, A. V. Vologzhanina, A. S. Belov, Y. Z. Voloshin and V. V. Novikov, *J. Phys. Chem. Lett.*, 2016, **7**, 4111–4116.
51 V. Novikov, A. A. Pavlov, Y. V. Nelyubina, M. E. Boulon, O. A. Varzatskii, Y. Z. Voloshin and R. E. P. Winpenny, *J. Am. Chem. Soc.*, 2015, **137**, 9792–9795.
52 T. J. Ozumerzifon, I. Bhowmick, W. C. Spaller, A. K. Rappé and M. P. Shores, *Chem. Commun.*, 2017, **53**, 4211–4214.
53 Y. Peng, T. Bodenstein, K. Fink, V. Mereacre, C. E. Anson and A. K. Powell, *Phys. Chem. Chem. Phys.*, 2016, **18**, 30135–30143.
54 S. Gómez-Coca, E. Cremades, N. Aliaga-Alcalde and E. Ruiz, *J. Am. Chem. Soc.*, 2013, **135**, 7010–7018.
55 Y. Y. Zhu, Y. Q. Zhang, T. T. Yin, C. Gao, B. W. Wang and S. Gao, *Inorg. Chem.*, 2015, **54**, 5475–5486.
56 M. R. Saber, M. K. Singh and K. R. Dunbar, *Chem. Commun.*, 2020, **56**, 8492–8495.
57 B. Yao, Y. F. Deng, T. Li, J. Xiong, B. W. Wang, Z. Zheng and Y. Y. Zhang, *Inorg. Chem.*, 2018, **57**, 14047–14051.
58 L. Cuevas-Contreras, M. M. Quesada-Moreno, E. Ruiz-Bilbao, J. M. Gutiérrez-Zorrilla, J. Krzystek, M. Ozerov, J.-R. Jiménez and E. Colacio, *Inorg. Chem. Front.*, 2026, **13**, 2882–2903 and references therein.
59 J. Zhang, J. Li, L. Yang, C. Yuan, Y.-Q. Zhang and Y. Song, *Inorg. Chem.*, 2018, **57**, 3903–3912.
60 Y.-Z. Zhang, S. Gómez-Coca, A. J. Brown, M. R. Saber, X. Zhang and K. R. Dunbar, *Chem. Sci.*, 2016, **7**, 6519–6527.
61 J. Li, Y. Han, F. Cao, R.-M. Wei, Y.-Q. Zhang and Y. Song, *Dalton Trans.*, 2016, **45**, 9279–9284.
62 P. Kalita, P. Kumar, M. M. Quesada-Moreno, E. Colacio and V. Chandrasekhar, *Chem. – Asian J.*, 2025, **20**, e202500062.

 This journal is © The Royal Society of Chemistry 2026

63 R. Mitsuhashi, K. S. Pedersen, T. Ueda, T. Suzuki, J. Bendix and M. Mikuriya, *Chem. Commun.*, 2018, **54**, 8869–8872.
64 S. Hazra, C. Rajnák, J. Titiš, M. F. C. Guedes da Silva, R. Boča and A. J. L. Pombeiro, *Molecules*, 2021, **26**, 1060.
65 N. Ahmed, P. Kalita, R. Nabi, T. Guizouarn, F. Pointillart, X. Zhang and V. Chandrasekhar, *Dalton Trans.*, 2025, **54**, 12648–12657.
66 J. Nehrkorn, J. Telser, K. Holldack, S. Stoll and A. Schnegg, *J. Phys. Chem. B*, 2015, **119**, 13816–13824.
67 S. Stoll and A. Schweiger, *J. Magn. Reson.*, 2006, **178**, 42–55.
68 A. K. Hassan, L. A. Pardi, J. Krzystek, A. Sienkiewicz, P. Goy, M. Rohrer and L. C. Brunel, *J. Magn. Reson.*, 2000, **142**, 300–312.
69 *APEX4*, Bruker AXS, Madison, Wisconsin (USA), 2022.
70 *SAINT, V8/40b*, Bruker AXS, Madison, Wisconsin (USA), 2021.
71 L. Krause, R. Herbst-Irmer, G. M. Sheldrick and D. Stalke, SADABS, Version 2016/2, *J. Appl. Crystallogr.*, 2015, **48**, 3–10.
72 G. M. Sheldrick, SHELXT-Integrated Space-Group and Crystal-Structure Determination, *Acta Crystallogr., Sect. A: Found. Adv.*, 2015, **71**, 3–8.
73 G. M. Sheldrick, Crystal Structure Refinement with SHELXL, *Acta Crystallogr., Sect. C:Struct. Chem.*, 2015, **71**, 3–8.
74 O. V. Dolomanov, L. J. Bourhis, R. J. Gildea, J. A. K. Howard and H. Pushman, OLEX2: A complete structure solution, refinement and analysis program, *J. Appl. Crystallogr.*, 2009, **42**, 339–341.
75 P. A. Malmqvist and B. O. Roos, *Chem. Phys. Lett.*, 1989, **155**, 189–194.
76 C. Angeli, R. Cimiraglia and J.-P. Malrieu, *Chem. Phys. Lett.*, 2001, **350**, 297–305.
77 C. Angeli, R. Cimiraglia, S. Evangelisti, T. Leininger and J.-P. Malrieu, *J. Chem. Phys.*, 2001, **114**, 10252–10264.
78 C. Angeli, R. Cimiraglia and J.-P. Malrieu, *J. Chem. Phys.*, 2002, **117**, 9138–9153.
79 F. Weigend and R. Ahlrichs, *Phys. Chem. Chem. Phys.*, 2005, **7**, 3297–3305.
80 A. Schaefer, H. Horn and R. Ahlrichs, *J. Chem. Phys.*, 1992, **97**, 2571–2577.
81 A. Schaefer, C. Huber and R. Ahlrichs, *J. Chem. Phys.*, 1994, **100**, 5829–5835.
82 F. Neese, *Wiley Interdiscip. Rev. Comput. Mol. Sci.*, 2022, **12**, e1606.
83 D. Ganyushin and F. Neese, *J. Chem. Phys.*, 2013, **138**, 104113.
84 D. Ganyushin and F. Neese, *J. Chem. Phys.*, 2006, **125**, 024103.
85 R. Maurice, R. Bastardis, C. D. Graaf, N. Suaud, T. Mallah and N. Guihéry, *J. Chem. Theory Comput.*, 2009, **5**, 2977–2984.
86 F. Neese, *J. Chem. Phys.*, 2005, **122**, 034107.
87 T. Nakajima, *Chem. Rev.*, 2012, **112**, 385–402.
88 J. Jung, M. Atanasov and F. Neese, *Inorg. Chem.*, 2017, **56**, 8802–8816.
89 M. Mikuriya, Y. Naka, A. Inaoka, M. Okayama, D. Yoshioka, H. Sakiyama, M. Handa and M. Tsuboi, *Molecules*, 2022, **27**, 4211.
90 T. Ivanova, A. Naumkin, A. Sidorov, I. Eremenko and M. Kiskin, *J. Electron Spectrosc. Relat. Phenom.*, 2007, **156–158**, 200–203.
91 M. Llunell, D. Casanova, J. Cirera, P. Alemany and S. Alvarez, *SHAPE, v2.1*, Universitat de Barcelona, Barcelona, Spain, 2013.
92 E. I. Stiefel and G. F. Brown, *Inorg. Chem.*, 1972, **11**, 434–436.
93 E. Baca-Solis, S. Bernès, H. Vazquez-Lima, M. E. Boulon, R. E. P. Winpenny and Y. Reyes-Ortega, *ChemistrySelect*, 2016, **1**, 6866–6871.
94 I. D. Brown, *J. Appl. Crystallogr.*, 1996, **29**, 479–480.
95 I. D. Brown and D. Altermatt, *Acta Crystallogr., Sect. B*, 1985, **41**, 244–247.
96 S. Griffith, *The theory of transition metal ions*, University Press, Cambridge, UK, 1961.
97 F. Lloret, M. Julve, J. Cano, R. Ruiz-García and E. Pardo, *Inorg. Chim. Acta*, 2008, **361**, 3432–3445.
98 N. F. Chilton, R. P. Anderson, L. D. Turner, A. Soncini and K. S. Murray, *J. Comput. Chem.*, 2013, **34**, 1164–1175.
99 J. Juráková, J. D. Midlíková, J. Hrubý, A. Kliuikov, V. T. Santana, J. Pavlik, J. Moncoľ, E. Čižmár, M. Orlita, I. Mohelský, P. Neugebauer, D. Gentili, M. Cavallini and I. Šalitroš, *Inorg. Chem. Front.*, 2022, **9**, 1179–1194.
100 N. Malinová, J. Juráková, B. Brachňaková, J. D. Midlíková, E. Čižmár, V. N. Santana, R. Herchel, M. Orlita, I. Mohelský, J. Moncol, P. Neugebauer and I. Šalitroš, *Cryst. Growth Des.*, 2023, **23**, 2430–2441.
101 S. Sottini, G. Poneti, S. Ciattini, N. Levesanos, E. Ferentinos, J. Krzystek, L. Sorace and P. Kyritsis, *Inorg. Chem.*, 2016, **55**, 9537–9548.
102 J. R. Pilbrow, *J. Magn. Reson.*, 1978, **31**, 479–490.
103 S. T. Liddle and J. van Slageren, *Chem. Soc. Rev.*, 2015, **44**, 6655–6669.
104 Y. F. Deng, T. Han, B. Yin and Y. Z. Zheng, *Inorg. Chem. Front.*, 2017, **4**, 1141–1148.
105 F. Neese, *J. Chem. Phys.*, 2007, **127**, 164112.
106 A. Singh and K.-N. Shrivastava, *Phys. Status Solidi B*, 1979, **95**, 273–277.
107 K.-N. Shrivastava, *Phys. Status Solidi B*, 1983, **117**, 437–458.
108 A. Lunghi and S. Sanvito, *J. Chem. Phys.*, 2020, **153**, 174113.
109 F. S. Santana, M. Perfetti, M. Briganti, F. Sacco, G. Poneti, E. Ravera, J. F. Soares and R. Sessoli, *Chem. Sci.*, 2022, **13**, 5860–5871.
110 M. Briganti, F. Santanni, L. Tesi, F. Totti, R. Sessoli and A. Lunghi, *J. Am. Chem. Soc.*, 2021, **143**, 13633–13645.
111 S. Nain, M. Kumar and M. E. Ali, *Phys. Chem. Chem. Phys.*, 2023, **25**, 15848–14861.

112 D. Aravena and E. Ruiz, *Inorg. Chem.*, 2013, **52**, 13770–13778.
113 B. Yin and C.-C. Li, *Phys. Chem. Chem. Phys.*, 2020, **22**, 9923–9933.
114 X. Wu, J.-F. Li and B. Yin, *Dalton Trans.*, 2022, **51**, 14793–14816.
115 Q.-Q. Yang, Y.-F. Wang, Y.-X. Wang, M.-J. Tang and B. Yin, *Phys. Chem. Chem. Phys.*, 2023, **25**, 18387–18399.
116 (*a*) CCDC 2573916: Experimental Crystal Structure Determination, 2026, DOI: 10.5517/ccdc.csd.cc2sdck4; (*b*) CCDC 2573917: Experimental Crystal Structure Determination, 2026, DOI: 10.5517/ccdc.csd.cc2sdcl5.

This journal is © The Royal Society of Chemistry 2026